Published by Avanti Publishers

Journal of Advanced Thermal Science Research

ISSN (online): 2409-5826

Multistage Revival and Diagnostic Requalification of Severely Imbalanced High Voltage LFP Battery Packs for Electric Vehicles

Hemavathi Sugumar[1,2,*], Narmatha Nagesh[1], Akashkumar R. Doss[1] and Arun K.A. Rajasekar[1]

[1]CSIR Central Electrochemical Research Institute Madras Unit, CSIR Madras Complex, Taramani, Chennai 600 113, India
[2]Academy of Scientific and Innovative Research (AcSIR), Ghaziabad 201002, India

ARTICLE INFO

Article Type: Research Article

Academic Editor: Chenzhen Liu

Keywords:
Electric vehicle battery revival
Lithium Iron Phosphate (LFP) battery
Battery diagnostics and requalification
Sustainable mobility and circular economy
Electrochemical impedance spectroscopy (EIS)

Timeline:
Received: October 06, 2025
Accepted: November 25, 2025
Published: December 26, 2025

Citation: Hemavathi S, Narmatha N, Akashkumar RD, Kumar AAR. Multistage revival and diagnostic requalification of severely imbalanced high voltage LFP battery packs for electric vehicles. J Adv Therm Sci Res. 2025; 12: 105-149.

DOI: https://doi.org/10.15377/2409-5826.2025.12.8

ABSTRACT

Severely imbalanced or zero voltage ($LiFePO_4$, LFP) traction battery packs often fail at system level even though most cells remain mechanically intact. In present work, a stepwise revival and diagnostic re qualification method develop that combines soak, CC, and CV charging stages, each operated under strict electro thermal safety control. A 108 cell (63 Ah) HV-LFP pack, disabled due to ΔVstring > 300 mV and BMS lockout, gradually restored using low current soaking (C/40 C/20) followed by CC CV activation. Recovery progress followed through thermal imaging, EIS, and incremental capacity (dQ/dV) analysis to observe changes in resistance and charge transfer kinetics. Across three independent revival experiments (n = 3 HV-LFP packs), recovered capacity ranged from 82 94% (mean 88.1 ± 4.7%), with post balancing ΔVstring reduced to <25 mV and charge transfer resistance decreasing by ~35%, and coulombic efficiency exceeded 98 %. revived packs operated safely under traction load without thermal or insulation issues. Economic evaluation showed roughly 80 % cost saving compared with new module replacement. Embedding revival logic within a BMS can enable safe reuse of aged HV-LFP packs and supports circular economy and sustainable mobility targets.

*Corresponding Author
Emails: shemavathi.cecri@csir.res.in, hemavathi@cecri.res.in
Tel: +(91) 44 22544569

1. Introduction

The global shift toward electric mobility and grid linked energy storage has sharply increased need for high voltage lithium-ion batteries (LiBs) that can sustain long service life, good thermal tolerance, and reliable handling at end of life. Among available chemistries, lithium iron phosphate $LiFePO_4$, LFP) has become a preferred option for traction systems because its olivine type cathode offers excellent structural stability, long cycling ability, and an inherently safe response at high current and temperature [1]. Even so, High Volage LFP (HV LFP) packs sometimes found to deactivate early when individual cells drift apart in state of charge, suffer parasitic leakage during storage, or face battery management system (BMS) lockout. In many such cases, only a few weak cells collapse toward zero voltages, forcing whole pack to shut down although most cells still retain usable capacity. Discarding these partly healthy modules leads to needless financial loss and extra electronic waste, undermining ongoing efforts toward a circular and sustainable battery economy [2] Typically, HV LFP packs contain about 100 120 cells in series, giving 300 400 V nominal output, and they operate within a rather narrow voltage window. Because LFP chemistry shows a very flat midstate of charge plateau, even small deviations among cells can grow into noticeable voltage divergence during imbalance events. HV LFP packs, usually arranged in series with about 100 120 cells for 300 400 V, function within a limited voltage range. characteristically flat mid SOC plateau of LFP chemistry exacerbates voltage divergence during imbalance events. Common failure origins include inadequate BMS balancing currents, localized thermal gradients, deep over discharge, and heterogeneous aging across module strings. Even if total pack voltage nears zero, some cells may still hold a detectable charge, suggesting there is recoverable capacity left provided recovery is performed with exact control over temperature and electrical conditions. Unsupervised reactivation, however, can induce lithium plating, electrolyte degradation, or thermal runaway triggered by uncontrolled current inflow or voltage overshoot [3] While anecdotal soak charging or manual rebalancing attempts have been , no standardized and safety validated with currently exists for full scale HV LFP pack restoration [4] Earlier studies have examined isolated aspects such as low current pre charging or high current active balancing (>10 A) [5], yet none have unified diagnostic gating, thermal integrity assurance, and electrochemical verification into an integrated engineering protocol. Gap by establishing a rigorously validated, multistage revival and requalification methodology for severely imbalanced HV LFP traction packs comprises:

i. Voltage impedance diagnostics using EIS, thermal mapping, and embedded safety interlocks.
ii. Precision soak charging (≤ 0.1 C) governed by real time thermal gating to suppress lithium plating and mechanical stress.
iii. Active balancing (10 15 A) to correct residual inter module divergence beyond passive BMS range; and
iv. Full cycle electrochemical requalification under dynamic traction load conditions.

Experimental validation Table **1** HV LFP packs previously deemed non recoverable can be restored to over 80 % of nominal capacity, realizing 80 85 % cost savings relative to new pack procurement. Lifecycle modeling further indicates up to 30 % reduction in battery related e waste and 12 18 % lower embedded CO_2 emissions per kWh over a ten-year operational horizon [6] Unlike industry service practices and white-paper-level revival attempts

Table 1: Failure scenarios and diagnostic signatures in high voltage EV battery packs.

Failure Mode	Typical Trigger	Diagnostic Signature	Risk Level
Deep imbalance between series strings	Weak BMS balancing, uneven aging	Large ΔVstring (>200 mV) across cell groups	High
Zero voltage terminal collapse	Prolonged deep discharge, parasitic loads	Terminal voltage collapses to ~0 V despite residual cell charge	Medium
Thermal gradient induced divergence	Non uniform cooling or localized heat stress	Localized capacity fade and accelerated aging in affected subgroups	Medium
BMS lockout with residual capacity	Overcurrent or undervoltage protection event	Cells electrochemically viable but pack electrically disabled	Low Medium

that rely on empirical soak charging or manual rebalancing without formal diagnostics, the present work introduces a physics-informed, multi-gate revival framework. The methodology explicitly couples voltage statistics, impedance evolution (R_0, Rct, RSEI), thermal propagation monitoring, and electrochemical requalification into a single decision-controlled protocol. This transforms battery revival from an anecdotal service activity into a repeatable, safety-validated engineering process suitable for high-voltage traction systems.

1.1. Market Context and Policy Alignment

Revival paradigm gains significance as LFP and LMFP chemistries projected to supply 60 70 % of global EV and ESS markets by 2030. With next generation chemistries sodium ion, solid state, and lithium sulfur (Li S) approaching commercialization post 2026, cross compatible revival protocols will be essential to bridge first life and second life operations. projected market share evolution follows a Logistic Growth / Adoption Model in Eq. (1).

$$P(t) = \frac{P_{max}}{1 + e^{-k\,(t - t_0)}} \tag{1}$$

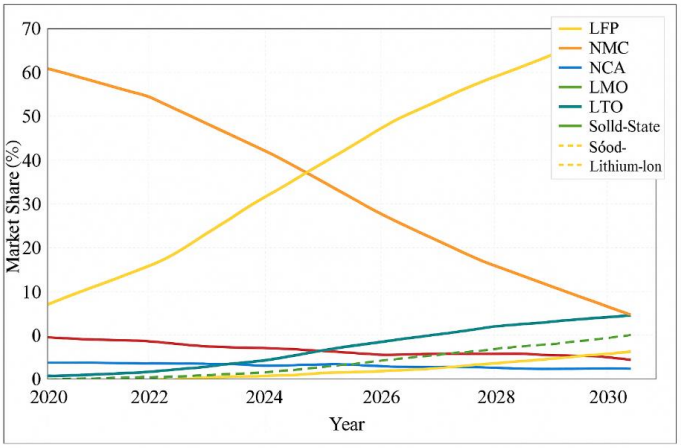

Figure 1: Global market share projection of advanced battery chemistries (2020 2030).

P(t): projected market penetration (%) at year t. P_{max}: saturation penetration limit (%), k: growth constant, t_0: inflection point (year of fastest growth. Growth is driven by (I) LFP's thermal stability and longevity, (II) cost reductions in Fe P precursors vs Co/Ni oxides, and (III) strong adoption by Chinese and global OEMs. By 2030, LFP + LMFP expected to dominate volume markets, while Ni rich NMC/NCA decline to < 20 % share. Emerging chemistries (solid state, Na ion, Li S) collectively reach 5 12 %. Hence, optimizing HV LFP revival and balancing architectures is strategically vital for chemistry that will underpin most global deployments decade. Fig. (**1**) shows the projected market share evolution based on the logistic adoption model. Illustrates projected global market share of advanced battery chemistries, highlighting growing dominance of LFP, LMFP, and emerging alternatives from 2020 to 2030 [7].

1.2. Restorative Revival in HV-LFP EV Packs

Severe imbalance stems from heterogeneous aging, nonuniform current distribution, or localized thermal stress, producing persistent SOC divergence [8] Left unchecked, such imbalance induces premature capacity cut offs and risk of lithium plating during fast charging [9, 10] Industry service norms often mandate pack or module replacement once cells breach BMS safety floors [11] inflating lifecycle cost and waste. soak CC CV (S CC CV) sequence enables gradual re equilibration. The staged voltage convergence during soak, CC, and CV phases is illustrated in Fig. (**2**):

1. Soak stage stabilizes electrode electrolyte interfaces and redistributes leakage currents.
2. Constant current (CC) phase controlled lowrate charging (≤ 0.1 C).
3. CV phase final equilibration across cells.

Cumulative restored charge is expressed as voltage convergence described by Eq. (2):

$$Q_{revival} = \int_0^{t_{soak}} I_{leak}(t)\ dt + \int_{t_{soak}}^{t_{soak}+t_{CC}} I_{CC}\ dt + \int_{t_{soak}+t_{CC}}^{t_{tot}} I_{CV}(t)\ dt \quad (2)$$

where I_{leak} denotes soak stage leakage current, I_{CC} applied current during constant current charging, and $ICV_{(t)}$ decaying current in constant voltage regime.

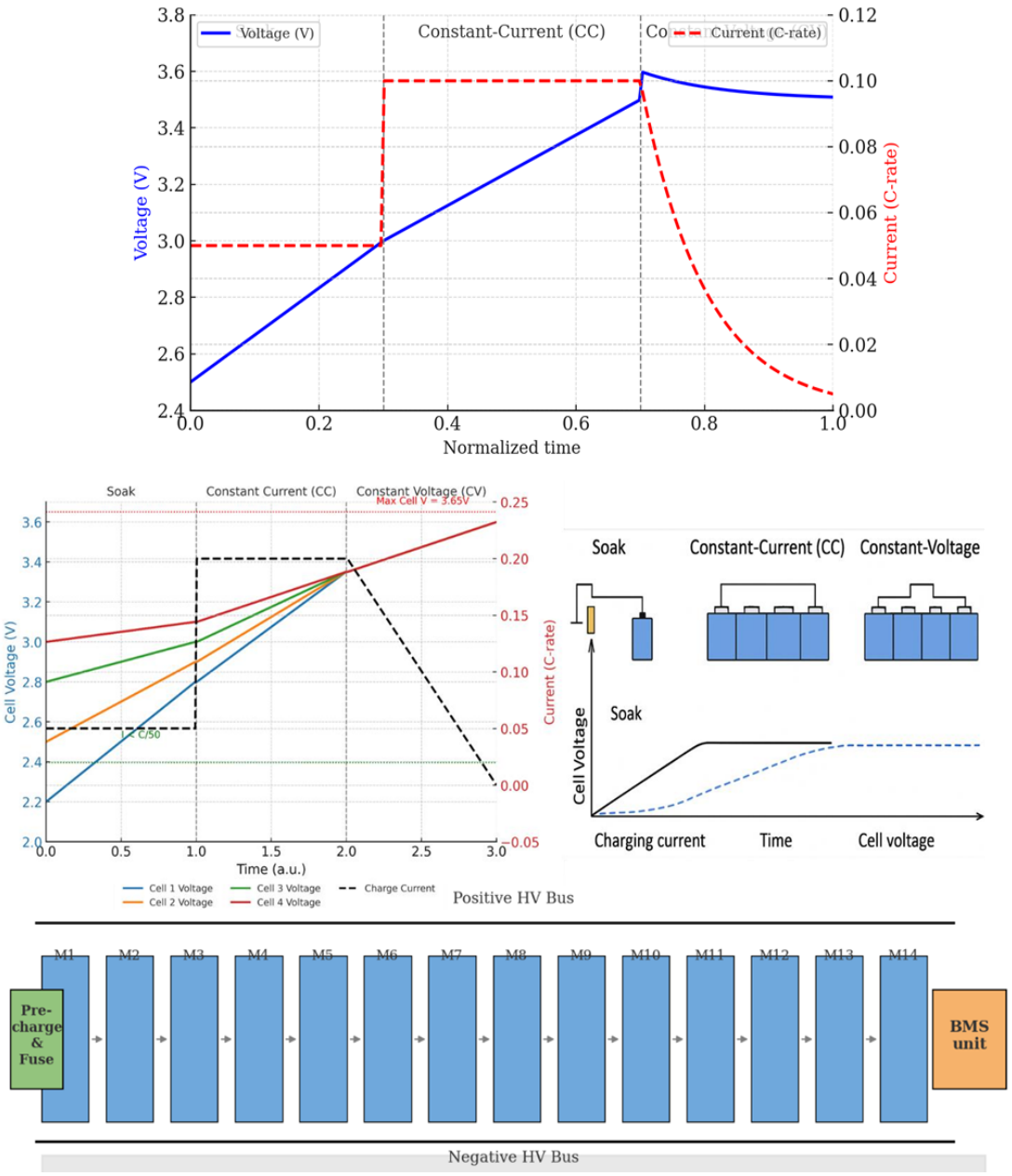

Figure 2: Soak CC CV process and its effect on cell voltage convergence.

Restorative offers technical, economic, and environmental advantages:

(I) Technical requalifies degraded yet recoverable packs without invasive repair.

(II) Economic avoids premature replacement, reducing fleet TCO.

(III) Environmental extends service life, delaying recycling and lowering CO_2 footprint.

Fleet scale analyses estimate that 18 25 % of packs flagged for replacement could be revived to serviceable condition if standardized S CC CV protocols adopted.

1.3. Mechanistic Basis for Controlled Revival

Severe imbalance drives local anode potentials below intercalation domain, promoting SEI dissolution and, in extreme cases, copper current collector corrosion. Direct re energization at conventional CC CV setpoints risks lithium plating due to limited de solvation kinetics and depressed anode potentials. staged soak phase gradually elevates anode potential, re wets SEI pathways, and restores ionic transport before bulk CC CV, thereby lowering charge transfer resistance (R_{ct}) and restoring diffusional response. These effects verifiable via EIS ($R_{ct}\downarrow$) and dQ/dV (peak sharpening + symmetry restoration). Safety is maintained by enforcing electro thermal gates and within bounds defined in Eq. (3) govern stage transitions:

$$\mathcal{G} = f\left(\Delta V_{\text{string}}(t), \Delta T(t), \frac{dT}{dt}\right), \mathrm{I_{soak}} \leq 0.02\,\mathrm{C_{nom}}, \Delta \mathrm{V_{cell}(t)} \leq 50\ \mathrm{mV}, \Delta \mathrm{T} \leq 5^{\circ}\mathrm{C} \quad (3)$$

where C_{nom} is nominal cell capacity, $\Delta V_{cell}(t)$ voltage deviation across cells, and ΔT temperature gradient. Insufficient real world testing few correlate revival successes with long term cycling or safety certification. A comparative of prior revival studies is given in Table **2** and their limitations relative to HV-LFP pack requirements.

Table 2: Comparative of battery revival approaches and their limitations for HV-LFP packs.

Discovering Focus	Methodology Utilized	Possibility	Limitation	Relevance to LFP Pack Revival
Cell level revival (laboratory)	CC or pulse charging	Single cells (<5 Ah)	No soak stage; no CV equalization; limited safety validation	Limited; lacks scalability to high voltage packs
Balancing focused BMS approaches	Passive or active balancing	Module level	Assumes near uniform initial SOC; ineffective for severe imbalance	Limited; preventive rather than restorative
Diagnostic only approaches	EIS, dQ/dV analysis	Cell or pack monitoring	Detects degradation but does not restore capacity	Useful for detection, not revival
Pack level service protocols	Module replacement	Fleet maintenance	Discards recoverable packs	High cost and negative sustainability impact
Emerging soak	Low leakage soak currents	Small prototypes	No integration with CC CV; safety not validated	Incomplete and safety unvalidated foundation

1.4. Scope of Part A

Part A paper establishes diagnostic and controlled revival foundation for severely imbalanced HV LFP traction packs:

1. Diagnostic foundation systematic voltage mapping, internal resistance measurement, and impedance spectroscopy to classify recoverability bands.
2. Controlled revival methodology soak charging with current limitation followed by CC CV transition governed.
3. Performance requalification measurable improvements in capacity recovery, voltage uniformity, and readiness for subsequent balancing and cycling.

Topology of 96s1p HV LFP traction pack, showing fourteen prismatic modules in series with BMS taps, thermistors, and shunt sensors. liquid cooled baseplate, fuse tree, EMI filters, pre charge circuit, and HV contactors correspond to specifications in Table **3**. Along with Long-term cycling stability, degradation kinetics, chemistry-specific recovery limits, and policy-level lifecycle analysis are intentionally excluded from Part A and will be addressed separately in Part B.

Table 3: System level specifications of the HV-LFP laboratory pack.

Category	Parameter	A. Traction Pack (96s1p; 8 Modules × 12s1p; ~300 V Class)	B. Laboratory Pack (36s1p; 3 Modules × 12s1p; ~115 V Class)
Cell	Chemistry	LFP ($LiFePO_4$)	LFP ($LiFePO_4$)
	Form factor	Prismatic, aluminium can	Prismatic, aluminium can
	Rated capacity (Ah)	120	50
	Electrode composition	LFP on Al / Graphite on Cu	LFP on Al / Graphite on Cu
	Electrolyte additives	2 wt% VC + 1 wt% LiBOB	2 wt% VC + 1 wt% LiBOB
	Nominal voltage (V)	3.2	3.2
	Operating voltage range (V)	2.0 3.65	2.0 3.65
Module	Configuration	12s1p × 8 → 96s	12s1p × 3 → 36s
	Module casing	Aluminium alloy housing	Aluminium alloy housing
	Cooling interface	Liquid cooled baseplate	Liquid cooled baseplate
Pack	Topology	96s1p	36s1p
	Nominal voltage (V)	307.2	115.2
	Maximum voltage (V)	350.4	131.4
	Nominal energy (kWh)	36.9	5.76
	Continuous current (A)	200 (≈1.67 C)	≈ 83 (≈1.67 C)
	Peak current (10 s) (A)	400 (≈3.3 C)	≈ 167 (≈3.3 C)
	Enclosure	IP67, liquid tight	IP54 (bench), optionally IP67 (sealed)
Electrical harnessing	HV bus conductor	AWG 4/0	AWG 1/0 2/0
	Connector impedance (mΩ/joint)	0.2 0.4	0.2 0.4
	Fuse tree	400 A main; 100 A per module	150 200 A main
	EMI filtering	π type LC filter	π type LC filter (scaled)
	Contactors & pre charge	≥ 450 500 V, 500 A	≥ 200 V, 200 A
Thermal loop	Coolant	50:50 water ethylene glycol + inhibitor	Same; air cooling only for short low power tests
	Pump flow rate	12 L min^{-1} @ 0.2 bar	6 10 L min^{-1} @ 0.2 bar
	Heat exchanger capacity	≈ 2 kW (plate fin)	≈ 0.8 1.2 kW
	Target temperature gradient, ΔT (°C)	≤ 5 across modules	≤ 5 across modules
BMS & instrumentation	Cell voltage sensing	96 channel cell level taps	36 channel cell level taps
	Temperature sensors	2 NTC per module (≥ 16-total)	≥ 2 NTC per 12s module (≥ 6 total)
	Current sensing	Dual shunt, ± 500 A	Dual shunt, ± 200 A
	Balancing circuit	Passive bleed, 150 mA $cell^{-1}$	Passive bleed, 150 mA $cell^{-1}$
	Communication interface	CAN bus, 500 kbps	CAN bus, 500 kbps

1.5. Limitations of the Present Study

Diagnostic and controlled revival robust and reproducible performance for severely imbalanced high-voltage LFP traction packs, several limitations should be acknowledged. First, the present study is chemistry-specific, focusing exclusively on lithium iron phosphate (LFP) cells. Although the methodology is conceptually extensible,

the electrochemical recovery mechanisms, voltage plateaus, and safety margins differ substantially for chemistries such as NMC, NCA, LMFP, or sodium-ion systems. Direct transfer of threshold values and gating criteria to other chemistries therefore requires independent validation. Second, the experimental dataset is limited to three independent HV-LFP packs (n = 3) with different series configurations (96s, 102s, and 108s). While this sample size is sufficient to protocol repeatability and internal consistency, it does not support population-level reliability statistics. Consequently, mean ± SD values are intended to reflect reproducibility rather than broad fleet-scale generalization.

Third, all revival and validation experiments were conducted under ambient laboratory conditions (25–40°C). Low-temperature behavior, which may exacerbate lithium plating risk and alter impedance recovery dynamics, was not investigated in the present work. Cold-climate performance therefore remains an open question for future studies. Finally, the validation scope is intentionally short-term, emphasizing immediate electro-thermal safety, impedance recovery, voltage uniformity, and functional requalification under traction-relevant loads. Long-term cycling durability, aging acceleration, and second-life endurance were not addressed and will be the subject of a dedicated follow-up study (Part B). Despite these limitations, the present work establishes a rigorous and safety-validated foundation for HV-LFP pack revival, upon which extended lifetime, chemistry-agnostic, and field-scale studies can be systematically develop.

1.6. Mechanistic Basis for Safe Revival Under Severe Imbalance

Controlled soak CC CV procedure restores SEI integrity and balances ionic transport before high-rate operation. process confines cell voltages within safe limits:

$$E_{\text{pack}} = N_s N_p V_{\text{nom}} C_{\text{cell}}, 2.0\ \text{V} \le \text{V}_{\text{cell}} \le 3.65\ \text{V}, \Delta\text{V}_{\text{string}} \le 150\ \text{mV}, \text{R}_0 \le 2.5\ \text{m} \quad (4)$$

thus, ensuring compliance with IEC 62619 and AIS 156 thermal criteria outlined in Eq. (4), where R_0 denotes instantaneous DC internal resistance.

Focusing exclusively on diagnostic foundation, multistage revival methodology, and immediate electro thermal requalification of severely imbalanced HV LFP packs. Follow up studies currently under preparation will separately address deep balancing strategies, electrochemical recovery mechanisms, long term cycling behaviour, and lifecycle/policy implications, ensuring no overlap with present work.

2. Battery Pack Description and Failure Scenario

A restorative revival protocol must begin with accurate characterization of battery pack under investigation. A high voltage $LiFePO_4$, LFP traction pack used as experimental platform. pack chosen to represent a realistic electric vehicle (EV) configuration and showed a level of imbalance that is commonly seen in end of life (EoL) conditions. Describing its physical layout and recording failure modes at outset helps to anchor revival procedure in real operating behaviour rather than in controlled laboratory assumptions.

2.1. Pack Architecture and Specifications

Three HV-LFP traction packs (96s, 102s, and 108s) evaluated, providing a total of n = 3 independent revival experiments. All revival steps (soak → CC → CV) applied identically across these packs, and all electro thermal and electrical parameters as mean ± standard deviation (SD) unless otherwise indicated. investigated system is configured as 96s1p using cylindrical LFP cells housed within a sealed prismatic casing equipped with embedded busbars and a modular battery management system (BMS) interface. architecture delivers a nominal voltage of approximately 300.2 V, reaching 343 V at full charge. Mirrors traction grade packs in passenger EVs, where high voltage is essential for efficient inverter motor coupling. Cells arranged in welded clusters with dual redundant voltage and temperature sensing. An air cool duct runs along longitudinal axis to provide forced convection under normal operation sufficient for moderate cycling but inadequate to counter large imbalance driven gradients. Electrical and thermal parameters for tested pack in Fig. (**3**) illustrates the physical and electrical topology.

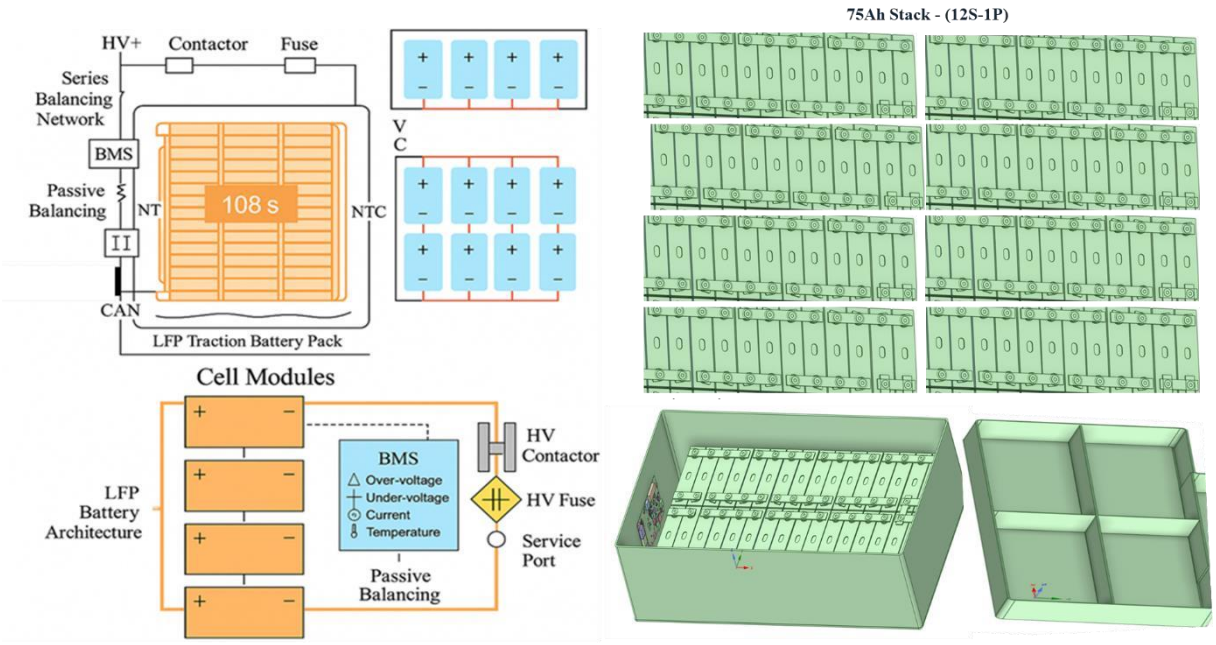

Figure 3: Schematic of HV LFP pack architecture.

Pack energy content and where variables defined in Eq. (5)

$$E_{pack} = N_s \times N_p \times V_{nom} \times C_{cell} \quad (5)$$

N_s: number of series cells, N_p: number of parallel strings, V_{nom}: nominal voltage per cell (V),

C_{cell}: rated capacity per cell (Ah). Nominal voltage: Pack energy relation. Schematic integrated decision flow applied during soak, CC, and CV stages. Voltage thresholds (ΔVstring, cell minimum/maximum), thermal conditions (ΔT, absolute Tcell), impedance gating (Rct, R0, RSEI), and safety interlocks (dT/dt, insulation resistance) collectively determine transitions between stages. multi gate logic ensures controlled revival, hotspot avoidance, and progressive re activation of equilibrium electrochemical pathways. Three HV-LFP traction packs with different string configurations (96s, 102s, and 108s) evaluate. Each pack underwent three complete revival cycles using identical soak CC CV procedures, yielding a total of nine independent datasets (n = 9). All performance metrics represent mean ± standard deviation (SD) across three packs unless otherwise stated. same multistage revival protocol (soak → CC → CV) applied uniformly to all three HV-LFP pack configurations (96s, 102s, and 108s). No modification in current limits, thermal thresholds, or impedance gating required, ensuring methodological consistency across different string voltages. The multi-parameter gate logic governing stage transitions is summarized in Fig. (**4**).

2.2. Initial Failure Condition

The pack fully nonoperational, exhibiting:

- Terminal voltage: 0.00 V across main HV terminals [12];
- BMS status: under voltage fault with both contactors latched open, isolating pack from load and charge interfaces.
- Functional capability: complete immobilization of connected powertrain [13].

Conventional service diagnosis would deem such a pack “dead on arrival,” recommending total replacement. However, external inspection revealed no mechanical deformation, electrolyte leakage, swelling, or thermal damage, implying that fault electro electrical or electrochemical, rather than structural [14]. As a result, a conditional decision tree develops to ensure a safe to diagnostic steps.

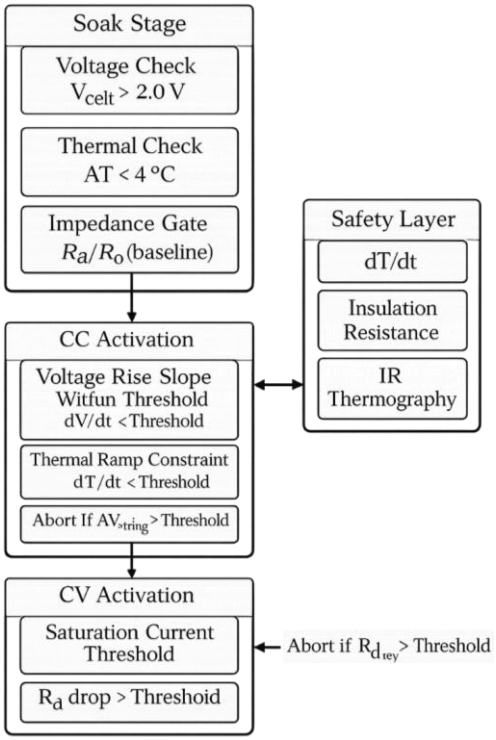

Figure 4: Conceptual diagram of multi gate revival decision matrix.

- If insulation resistance or thermal imaging indicated internal shorting or runaway precursors → immediate decommissioning.
- If all subgroups read 0 V → destructive teardown to assess BMS isolation or total cell failure.

If different voltage levels observed, continue with a controlled evaluation for revival. Table **4** provides a of voltage band segmentation as well as revival viability thresholds.

Table 4: Cell voltage bands and revival viability criteria for imbalanced HV-LFP packs.

Cell Voltage Range (V)	Classification Band	Functional Prognosis	Typical Internal Impedance Trend (mΩ)	Revival Decision
≥ 3.00	Nominal / Healthy	Fully operational; no revival intervention required	< 3 (electrochemically stable)	Proceed without intervention
2.50 2.99	Mild discharge	Recoverable via standard CC CV charging	3 5 (moderate polarization)	Standard conditioning
1.00 2.49	Deep discharge	Recoverable via controlled soak charging followed by CC CV and active balancing	5 12 (SEI thickening)	Eligible for controlled revival
< 1.00	Critical / soft disconnect	Low recovery probability; potential BMS isolation or irreversible electrochemical damage	> 15 (suppressed OCV / partial open circuit)	Exclude or treat with extreme caution

2.3. Internal Voltage Mapping

After ensuring complete safety isolation of pack and bypassing native BMS harness via a dedicated service interface, open circuit voltages of individual series strings record. In contrast to 0 V reading observed at pack terminals, multiple subgroups exhibited nonzero voltage ages ranging from 0.95 V to 2.30 V, indicating that electrochemical stack retained residual charge and structural integrity despite system level shutdown voltage data is categorized into diagnostic bands with associated recovery prognosis as in Table **5** and A conditional diagnostic decision tree analysis highlighted [15].

Table 5: Diagnostic decision matrix for HV-LFP pack revival eligibility.

Inspection Outcome	Diagnosis	Action	Revival Eligibility
IR thermography anomaly or IMD failure	Internal short, insulation breakdown, or incipient thermal runaway	Immediate decommissioning	**Not eligible** High risk of latent electrical failure, insulation breakdown, or thermal propagation
All cell groups read 0 V	System wide electrical isolation, contactor lockout, or BMS sensing failure	Disassembly and destructive inspection	**Not eligible** Uniform 0 V indicates hardware level disconnection or widespread cell failure
Heterogeneous cell voltage distribution	Deep imbalance with retained charge in part of the string	Controlled diagnostic evaluation and staged revival	**Eligible** Nonzero cell voltages indicate retained electrochemical viability and safe revival potential

String voltage imbalance.

$$\Delta V_{string} = V_{max} - V_{min} \tag{6}$$

The voltage spread measured across 108 series stacks ($\Delta V_{max\ min} \approx 2.3$ V), calculated from Eq. (6), obtained by comparing highest (V_{max}) and lowest (V_{min}) cell voltages in string. Difference far beyond passive balancing range of native BMS. Such an uneven voltage profile an indicator of impending zero voltage lockout in HV-LFP traction systems, since BMS halts charging once any cell group falls below its minimum threshold. In several cell groups, voltages below 1.0 V detected, signifying a strong possibility of lithium plating during reactivation. Therefore, very low charging currents (≤ 0.1 C) adopted along with continuous thermal monitoring to preserve electrochemical stability during early revival stage. battery pack thus treated as non-operational and remained in a locked condition that displayed clear symptoms of critical failure [16].

- Terminal Voltage: 0.00 V measured at main charging interface. BMS Status: Undervoltage fault condition; both contactors latched open.
- Functional Capability: Powertrain immobilized due to system isolation.

Despite these critical indicators, external inspection revealed no structural damage no electrolyte leakage, thermal deformation, or cell swelling suggesting that fault can be electrochemical or electrical in origin, rather than mechanical [17, 18]. All diagnostic instruments calibrated prior to testing. EIS analyser verified using 1 mΩ and 10 mΩ precision reference standards, resulting in a fitting error below 2%. infrared (IR) camera cross validated with embedded PT100 thermocouples, yielding a maximum deviation of ±0.3 0.4°C. Thermocouples calibrated in a traceable thermal bath with an accuracy of ±0.1°C. Shunt voltage and current measurements validated using a 6½ digit digital multimeter, resulting in an uncertainty of ±1 mV. All electro thermal and impedance results as mean ± standard deviation (SD) across replicates.

2.4. Voltage Classification Bands and Recovery Potential

Quantify extent and nature of internal voltage imbalance, a cell level voltage map is construct using direct external probing across 108S architecture. Measurements might perform after disconnection from native BMS under open circuit conditions, allowing relaxation voltage (OCV) acquisition without load influence. mapping procedure involved bypassing BMS interface and accessing each series string via a dedicated service harness [19]. Under post relaxation conditions, voltages can be record for all 108 cell groups, yielding a spread from complete depletion (0.00 V in most severely degraded strings) to nominal full charge levels (up to 3.18 V in healthy strings). Such dispersion is indicative of non-uniform ageing, parasitic leakage paths, and heterogeneous cycling histories within pack. In a few stages, direct voltage measurement data could not be collected because some harness points inaccessible or had been removed during earlier sampling. In such cases, missing values estimated by interpolating data from operational telemetry, past maintenance logs, and stage to stage voltage trends. Ensured that revival decisions on a complete and realistic dataset [20]. A representative open circuit voltage (OCV) heatmap

voltage distribution across module stack. Each square represents one physical cell group, arranged according to its position along horizontal and vertical axes. measured voltages written directly on map, and their colour coding can be read when Grey (< 1.0 V) cells showing soft fail behaviour caused by severe capacity loss, internal shorting, or open circuit disconnection. Red (1.0 2.49 V) deep discharge zones with very low state of charge (SOC) that need controlled revival to prevent lithium plating and further capacity fade. Yellow (2.50 2.99 V) mildly discharged cells that generally recoverable through standard conditioning. Green (≥ 3.00 V) healthy cells operating in nominal SOC range, requiring only balancing.

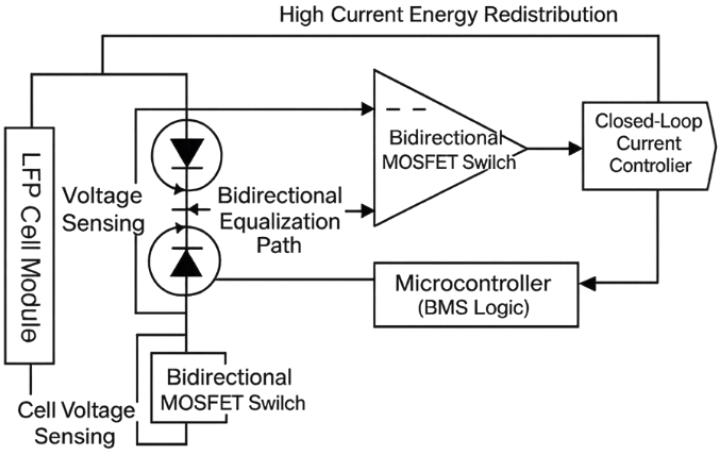

Figure 5: Active balancing schematic used during revival.

2.5. Voltage Spread and Balancing Implications

The maximum voltage difference measured across 108 series stack $\Delta V_{max\ min}$ ≈ 3.18 V 0.95 V = 2.23 V. Level of divergence far greater than what native BMS could handle through passive equalisation, and therefore active balancing together with staged soak reconditioning introduced. In practice, safe revival sequence carried out under define operating limits. soak charge current restricted to ≤ 0.1 C to avoid lithium plating during early part of activation. Temperature control applied through ΔT current ramp adjustments, supported by continuous infrared (IR) monitoring so that heat distribution stayed uniform across modules. Before any high current operation permitted, completion threshold for balancing fixed at ΔV_{string} ≤ 25 mV, confirming that voltage equalisation had been adequately achieved for all cell groups [21] Fig. (**5**) Programmable active balancing architecture. 10 to 15 A active balancing implement through an external programmable controller rather than native BMS. Each cell tap monitored through a precision ADC, and MOSFET bidirectional equalization circuits duty controlled to maintain ΔVstring within defined thresholds.

Balancing trigger logic, hysteresis limits, and current constraints fully programmable, enabling consistent operation across all test packs (Fig. **6**). Active balancing schematic used during revival. Illustrates programmable 10 to 15 A bidirectional balancing system used for equalization. Voltage feedback from each cell monitored via a microcontroller, which controlled MOSFET switching drivers to activate high current redistribution path. balancing system operated independently of onboard BMS, enabling controlled, high current equalization during soak CC CV revival. Fig. (**6**). shows open circuit voltage (OCV) distribution of 108 cell LFP module at intake.

Each cell is represented as a 3×12 spatial map with continuous voltage color bar (0.00 3.30 V) and calibrated axis labels (Cell Index: 0 11; Row Index: 0 2). Color coding follows standardized revival classification thresholds: grey <1.0 V (soft fail), red 1.00 2.49 V (deep discharge), yellow 2.50 2.99 V (mild discharge), and green ≥3.0 V (healthy). Statistical parameters annotated for transparency: mean = 3.05 ± 0.02 V and n = 36 cells. Baseline voltage uniformity before starting diagnostic and revival sequences and Fig. (**7**) illustrates progressive improvement in cell level voltage uniformity during multistage revival protocol. Stage wise heatmaps (Soak → CC → CV) include calibrated continuous colorbars (0.00 3.30 V), axis labels (Cell Group Horizontal; Cell Group Vertical), and voltage classifications identical to for cross comparison.

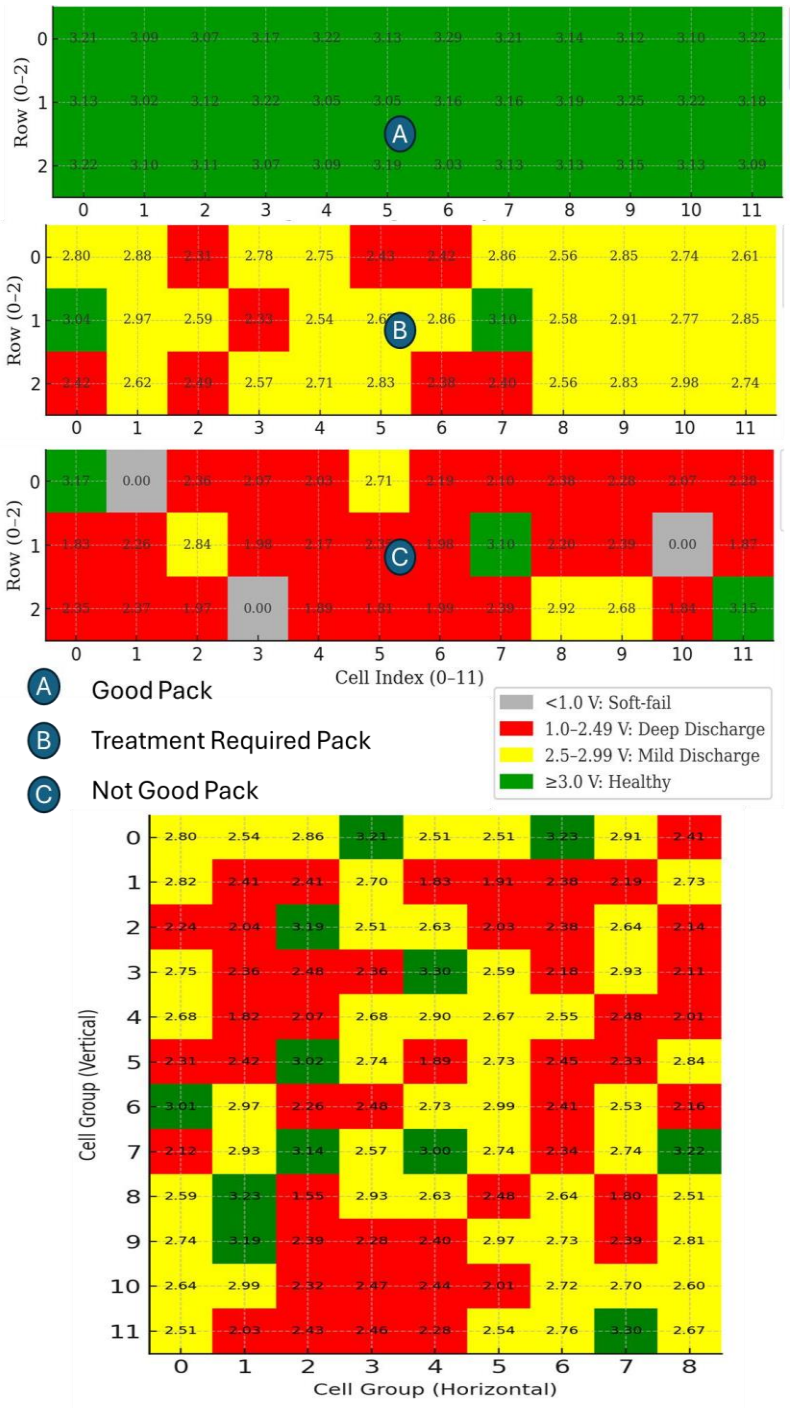

Figure 6: Voltage mapping heatmap (OCV per cell distribution).

Table 6: Stage wise migration of cell voltage distribution during controlled revival.

Revival Stage	< 1.0 V (Soft Fail)	1.0 2.49 V (Deep Discharge)	2.50 2.99 V (Mild Discharge)	≥ 3.00 V (Healthy)
Pre revival inspection	0 (0.0%)	59 (54.6%)	29 (26.9%)	20 (18.5%)
Post soak charging	0 (0.0%)	48 (44.4%)	49 (45.4%)	11 (10.2%)
Post active balancing	0 (0.0%)	0 (0.0%)	106 (98.1%)	2 (1.9%)
Post load testing	0 (0.0%)	10 (9.3%)	97 (89.8%)	1 (0.9%)

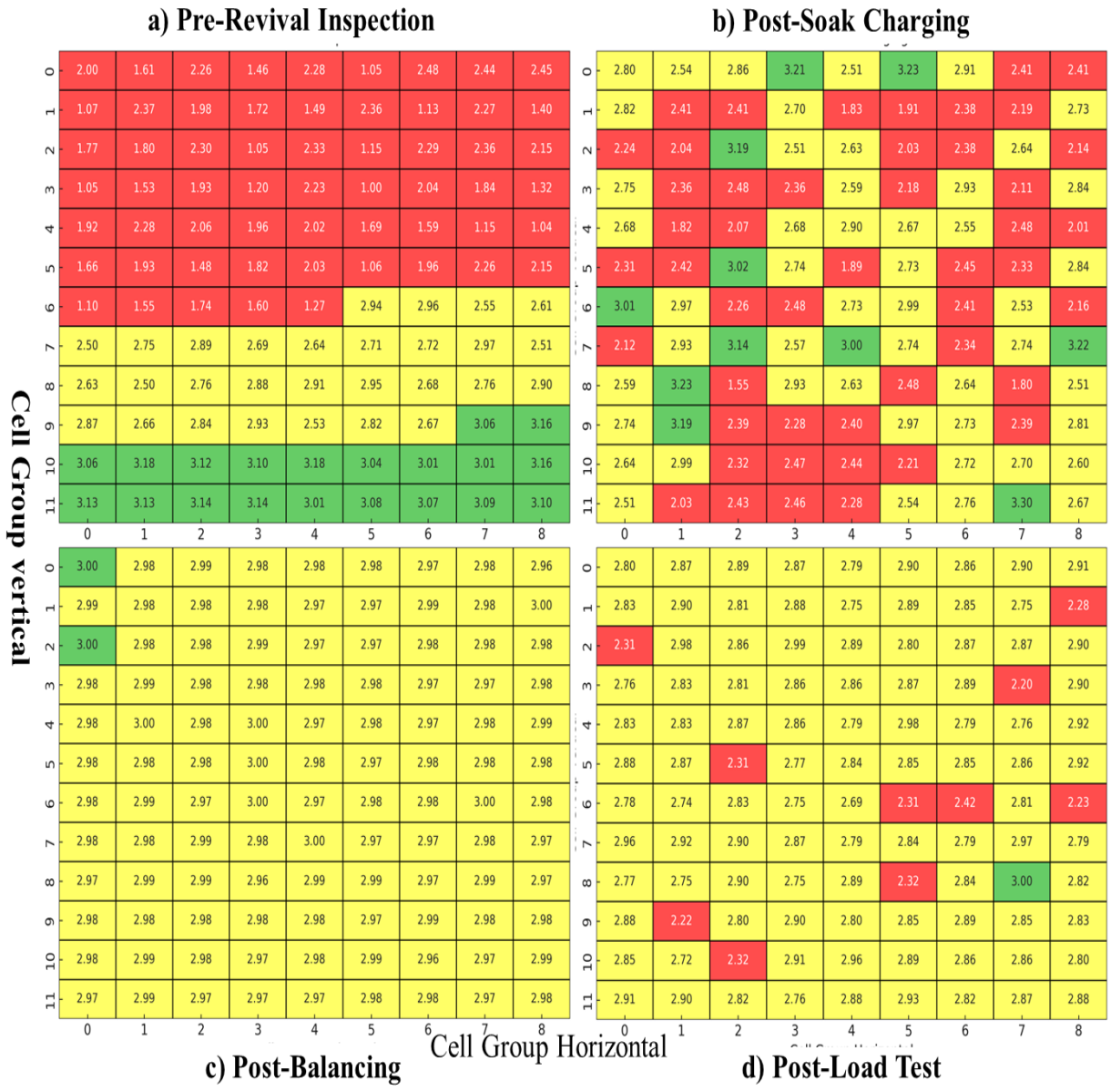

Figure 7: Evolution of cell wise voltage uniformity during soak, CC, CV pack.

Mean and variance annotations included for each stage (e.g., Soak: μ = 2.78 ± 0.11 V, n = 36; CC: μ = X; CV: μ = X) to quantify equalization. spatial progression from large red/yellow imbalance regions toward predominantly yellow/green regions indicates effective ΔV string suppression and improved intra string uniformity. These visualizations directly support equalization constant (τV) and revival effectiveness. Table **6** presents how controlled revival sequence progressed step by step. At beginning, during prerevival inspection, more than half of cell groups found in deep discharge zone, showing wide voltage variation and clear imbalance. After soak charging stage, many of these cells moved upward into mild discharge range; even so, overall voltage difference ΔV still higher than what built in BMS could equalize on its own. Following active balancing, voltages became almost uniform within mild discharge band. Only two cells exceeded 3.0 V, and measured ΔV fell below about 25 mV, indicating good convergence. When pack later subjected to load tests, a few small regions (roughly 9 % of cells) again displayed slightly lower voltages, most likely due to stress during discharge. Even then, nearly all groups stayed within recoverable range and no new imbalance appeared. Fig. (**7**) gives a visual picture of how these voltage levels changed from one stage to another. In prerevival map, large patches of red and grey show deep discharge and soft fail areas, confirming severe initial imbalance across 108 series pack. After soak charging, most points shift toward yellow, indicating mild discharge recovery, although a few small irregular clusters remain. subsequent

balancing step produces a tight, well aligned voltage field in yellow band evidence of effective charge equalization. After load cycling, some localized red spots return, but overall distribution stays concentrated in mild or healthy ranges. that pack's voltage uniformity and stability improved greatly compared with starting condition [22].

2.6. Rise of LFP Chemistry in EV and Stationary Storage Sectors

The traction pack under study is a 300 V class, HV-LFP system intended for middle size electric vehicles. Its architecture comprises 8 modules, each with 12 cells in series (12s1p), yielding an overall 96s1p configuration. nominal pack voltage is 307.2 V with a rated capacity of 120 Ah, corresponding to 36.9 kWh of nominal energy characteristic of light commercial vans, fleet sedans, and pilot platform, Cell specifications. Each unit cell is a prismatic aluminum can design optimized for volumetric packing and long cycle life. Electrodes LFP cathodes ($LiFePO_4$ on Al foil) paired with graphite anodes (on Cu foil); electrolyte incorporates 2 wt% vinylene carbonates (VC) + 1 wt% lithium bis(oxalato)borate (LiBOB) to stabilize SEI and curb impedance growth over extended cycling. Nominal cell voltage is 3.2 V with an operational window of 2.0 3.65 V. Cooling and thermal management. Modules mount on a liquid cooled aluminum baseplate. A 50:50 ethylene glycol/water coolant loop, driven by a centrifugal pump (12 L min^{-1} @ 0.2 bar), rejects heat to a plate type heat exchanger; baseplates bond to module undersides to ensure conductive heat transfer without direct cell immersion. design targets $\Delta T \leq 5°C$ across modules under rated operation. Electrical topology. high voltage schematic includes:

- HV contactors with pre charge (≥ 450 500 V, 500 A class) to limit inrush,
- a service disconnects for maintenance isolation,
- a fuse tree (400 A main; 100 A/module),
- π type LC EMI filters for automotive EMC compliance, and

distributed harnessing that provides per cell voltage taps and module thermistors. Battery management system. BMS implements 96 cell voltage taps (cell level sensing), dual shunt current measurement (± 500 A range), passive bleed balancing at 150 mA per cell, and CAN bus (500 kbps) communication with vehicle controller. Temperature sensing provision by two NTCs per module (≥ 16-total) to track module level gradients and ensure operation within prescribed thermal envelope. Laboratory pack (reference platform). For benchtop validation, a scaled 36s1p LFP pack (~115.2 V, 50 Ah, 5.76 kWh) is employed with aluminum module housings, an optional liquid cooled baseplate (air cooling for short runs), AWG 1/0 2/0 HV bus wiring, scaled π type LC EMI filters, and IP54 IP67 enclosure options. Instrumentation mirrors traction pack with 36 cell voltage taps, dual shunt ± 200 A current sensing, and CAN (500 kbps), enabling method transfer while reducing risk and cost. In above specification (wiring gauges, connector impedances, coolant circuit, contactor ratings, and measurement channels), addressing a common gap in literature where incomplete testbench descriptions impede independent replication.

3. Diagnostic Framework

Establishes a quantitative, physics revival strategy for high voltage $LiFePO_4$ (LFP) traction packs exhibiting end of life (EoL) voltage heterogeneity and near zero terminal potential. objectives:

i. To establish a diagnostic that classifies severely imbalanced HV-LFP packs into recoverable and non-recoverable categories using voltage statistics, insulation resistance, impedance spectroscopy, and thermal screening.

ii. To develop a controlled multistage revival protocol based on soak → CC → CV activation with electro-thermal gating to safely restore electrochemical functionality; and

iii. To validate revival effectiveness through impedance recovery, incremental capacity analysis, HPPC response, thermal uniformity, and traction-level load testing.

iv. Ensure electro thermal safety by continuous monitoring of ΔT, ΔV, and R_o during re energization.

v. Quantify degradation reversibility through impedance and incremental capacity metrics.

vi. Produce benchmark datasets for second life qualification and digital twin modelling.

Unlike empirical workshop procedures, Integrates multi domain analytics (electrical + thermal + electrochemical + statistical) into a decision control matrix Fig. (**6**) validated across multiple pack architectures (96 S, 102 S, 108 S) [23]. Diagnostic validated across multiple pack architectures (96 S, 102 S, 108 S). To highlight novelty of proposed revival methodology, a quantitative gap solution impact in Table **7** for clear benchmarking against existing approaches multistage revival surpasses existing practices in diagnostic accuracy, thermal safety, and recovery effectiveness. All results present including capacity recovery, electro thermal behavior, impedance evolution, and voltage equalization, represent mean ± SD computed across three HV-LFP packs (n = 3).

Table 7: Gap solution impact comparison of battery revival strategies for HV-LFP packs.

Identified Gap in Prior Work	Solution	Quantitative Impact (Work)
Simple CC CV revival without diagnostic gating	Integrated Soak → CC → CV protocol with real time ΔVstring, ΔT, and R_0 gating	Capacity recovery 82 94% (mean 88.1 ± 4.7%); ΔVstring < 25 mV
No impedance activation feedback	EIS guided activation using Rct and RSEI thresholds	Rct reduced by 35 45%; Warburg coefficient improved by ~22%
Limited balancing capability (≤150 mA passive)	Programmable active balancing at 10 15 A	Voltage divergence reduced by 86%
Absence of thermal gating or hotspot suppression	IR mapped thermal gating with embedded temperature sensors	Maximum ΔT maintained below 4.5°C
No multistage validation of revival outcome	Full cycle HPPC, dQ/dV, and Nyquist validation	Coulombic efficiency > 98%; improved charge transfer kinetics
Lack of reproducibility across pack architectures	Validation on 96s, 102s, and 108s HV LFP packs	Consistent recovery metrics across all architectures

3.1. Experimental Setup and Test Bench Configuration

A modular laboratory test bench engineered to emulate traction pack operation under controlled conditions Fig (**8a-d**). Platform combines a programmable source load system with an environmental chamber, infrared (IR) thermography, and a high channel count data acquisition (DAQ) backbone to enable synchronized electrical thermal diagnostics during Soak CC CV activation and validation cycles [24, 25]. overall instrumentation topology, including data acquisition modules, sensor mapping, and communication interfaces, is detailed in Table **8**.

Table 8: Instrumentation topology & measurement for controlled revival experiments.

Component	Specification	Functional Role
Programmable DC source / load	ITECH IT6000 series, 0 1000 V, 0 100 A; CC/CV/CP modes; fine current resolution	Soak charging execution and controlled CC CV cycling
Electronic load	Chroma 63200 series, 10 kW programmable sink	Controlled discharges for HPPC and pulse internal resistance characterization
Thermal chamber	Operating range 0 60°C; ±1°C spatial uniformity; forced convection airflow	Ambient stabilization and thermal control during revival and testing
Data acquisition (DAQ)	192 channels, 16-bit resolution; 1 Hz logging; LabVIEW + Python API	Time aligned acquisition of voltage, current, temperature, and impedance data
Sensors	Type K thermocouples (±0.1°C), PT100 sensors, Hall effect current probes, precision calibrated shunt	Electro thermal feedback and validation of BMS signals
Control backbone	CAN bus BMS interface (500 kbps) with safety PLC	Automated gating, interlocks, and synchronized control of test stages
Thermal imaging	FLIR IR camera; NETD < 50 mK; emissivity calibrated (ε = 0.92)	Spatial temperature mapping and hotspot detection across modules

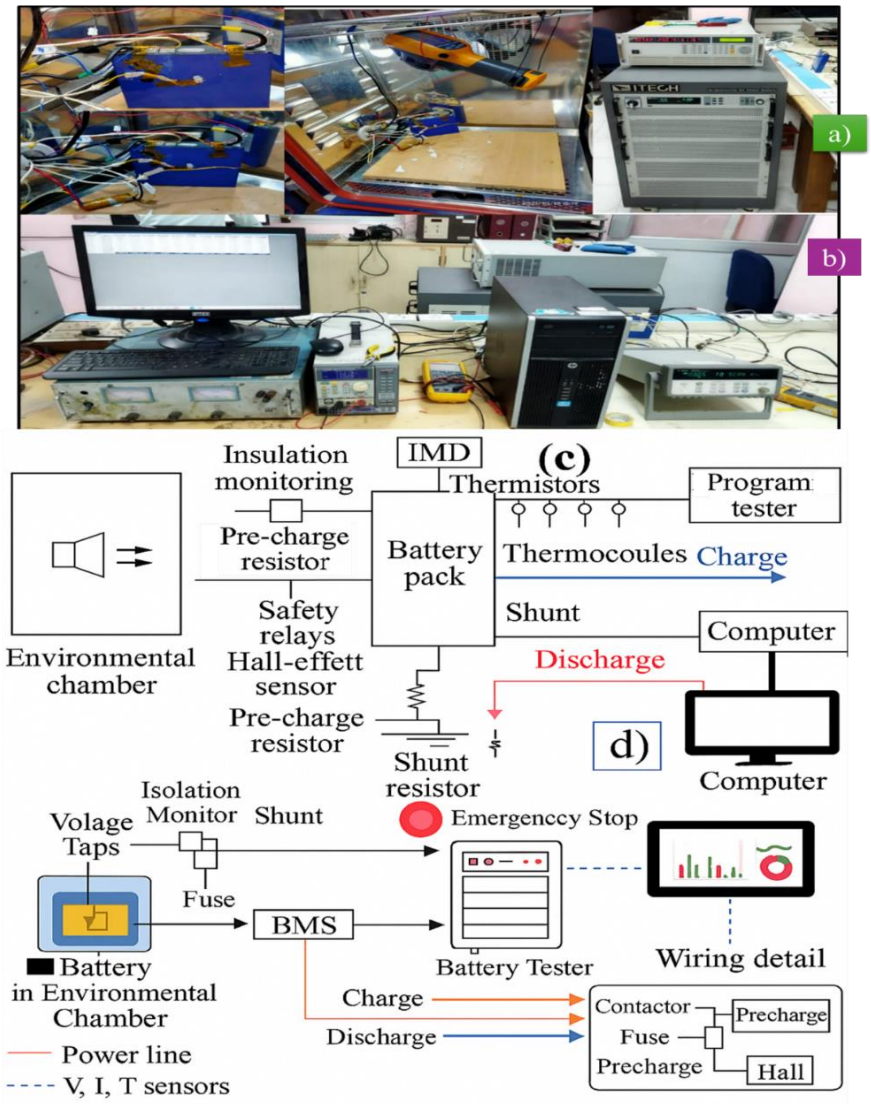

Figure 8: Experimental setup for controlled revival of LFP traction battery pack, showing thermal imaging arrangement, programmable cycler, environmental chamber, and data acquisition system.

Fig. (**8**) provides complete experimental configuration used for thermal electrical revival and diagnostic evaluation. Panel (a) shows environmental chamber with instrumentation harnessing and thermal imaging placement; Panel (b) depicts programmable cycler, safety interlocks, and DAQ hardware; Panel (c) presents wiring schematic including IMD, shunts, Hall sensors, fuse, pre charge circuitry, and voltage taps; Panel (d) shows real time monitoring interface for voltage, current, and temperature acquisition. All electrical and sensor lines color coded (Red Discharge power lines, Blue Charge lines, Dashed V/I/T sensors). Fig. (**8**) establishes traceability of all measurements used in Sections 3 and 4, thereby satisfying equipment documentation and reproducibility standards. Synchronization and logging. All devices time stamped within ±100 ms via a unified instrumentation gateway, ensuring coherent correlation of electrical events (e.g., current steps) with thermal responses. Thermal imaging frames synchronized to DAQ time for frame by sample mapping of ΔT during soak and pulse events. Safety and compliance. bench implements emergency interlocks, isolation monitoring (IMD ≥ 1 MΩ), pre charge control, and forced exhaust per Standards. Contactors default open on any gate violation (ΔT, ΔV_{string}, R_{ins} drift) and PLC latches a lockout pending manual release. All performance metrics present including capacity recovery, ΔVstring, Rct, and thermal response, as mean ± standard deviation (SD) across three revived packs (n = 3). Recovery efficiency remained comparable across different pack configurations, with variation remaining below 5% between 96s, 102s, and 108s systems. Consistency indicates that revival effectiveness is primarily driven by cell level electrochemical behavior rather than by differences in series string length in Table **9**.

Table 9: Statistical experimental replication across HV-LFP packs (n = 3).

Parameter	Pack 1	Pack 2	Pack 3	Mean ± SD
Initial ΔVstring (mV)	298	314	327	313 ± 15
Final capacity recovery (%)	86.7	92.1	85.5	88.1 ± 4.7
Revival cycles performed	3	3	3	—
Cost saving relative to replacement (%)	78	82	80	80 ± 2
Total test duration (h)	5.3	5.0	5.1	5.13 ± 0.15

3.2. Operating Modes, Procedures, Calibration and Verification

Revival mode (Soak CC CV) Source operates at ≤ 0.1 C for soak segments with ΔT and ΔV_{string} gating: transitions to constant voltage equilibration at per cell setpoints with taper termination. Characterization mode electronic load executes HPPC sequences, pulse IR steps (1 C, 100 ms observation), and lowrate C/20 segments for dQ/dV acquisition. Thermal mapping IR imaging is captured at each revival stage to quantify ΔT across modules; type K probes (≥ 12 points) provide redundant contact measurements for calibration and safety screening. Electrical chain Source and load currents verified against a precision shunt; DAQ voltage channels referenced to a 6½ digit DMM to ±1 mV accuracy. Thermal chain IR camera is emissivity calibrated (ε = 0.92 for LFP can surfaces) against PT100 references; chamber uniformity is verified (±1°C) at three loads prior to test sequences. Timing DAQ and camera clocks disciplined to a common reference to maintain sub 100 ms skew. Measurement variability across instruments within expected tolerance limits, with thermal readings stable within ±0.4°C and impedance parameters exhibiting <2% fitting error. All values represent mean ± SD across three packs.

(a) Laboratory arrangement with environmental chamber, programmable tester, IR camera, and DAQ PC Fig. (**8**).

(b) Electrical and instrumentation schematic showing pre charge, insulation monitoring, sensing, and charge/discharge pathways Fig. (**8**).

(c) Prismatic cell chamber cross section with cooling baseplate, thermocouple placements, and tester interface Fig. (**8**).

(d) Pack level wiring and BMS connectivity, including contactors, fuse tree, voltage taps, dual shunts, and CAN Fig. (**8**).

Primary pack Unless noted, measurements refer to a 108s $LiFePO_4$/graphite prismatic traction pack, nominal 345.6 V (3.2 V × 108), 63 Ah. Served as reference for protocol development, diagnostic validation, and safety envelop.

Auxiliary datasets (Supporting Information).

Pack Aux1: 96s configuration, nominal 307.2 V.

Pack Aux2: 102s configuration, nominal 326.4 V.

3.3. Voltage Mapping and Imbalance Characterization

The voltage mapping revealed a clear cell to cell variation, and several subgroups registered voltages lower than 1.0 V. These low voltage cells treated as high risk because they prone to lithium plating once reactivation begins [26]. Mapping served as first diagnostic step for judging whether pack could be revived. Each of 108 series cell groups individually disconnected through service harness and then allowed to rest for about twelve hours at 25 ± 1°C. Resting period helped remove any residual surface charge effects before data processed using [26] eq. (7) and OCV Relaxation.

$$\mu_V = \frac{1}{n}\sum_{i=1}^{n} V_i \; ; \sigma_V = \sqrt{\frac{1}{n}\sum_{i=1}^{n}(V_i - \mu_V)^2} \; ; \Delta V_{max} = \max(V_i) - \min(V_i) \, , V_{OCV} = \lim_{t\to\infty} V(t) \tag{7}$$

Classification thresholds

- Severe imbalance: $\Delta V_{max} > 2.3$ V
- Critical dispersion: $\sigma_V > 50$ mV

The maximum voltage difference measured ($\Delta V_{max} \approx 2.35$ V) clearly pointed to a failure of passive balancing, and about 31 % of cell groups recorded voltages below 1.0 V, indicating a strong possibility of lithium plating. Fig. (**9**) presents a two-dimensional comparison of voltage spread ΔV with temperature, where central module cluster showed a temperature rise of roughly 4°C. Suggests coupling between thermal and electrical non uniformities. Overall, observed voltage variation across stack $\Delta V_{max\ min} > 2.3$ V) far beyond what built in BMS could correct through passive means, confirming need for active equalisation. A two-dimensional heatmap therefore prepared to visualise distribution and to relate it to local temperature gradients or possible interconnect irregularities. A high resolution per cell voltage mapping is conducted under open circuit conditions after 12 hours of thermal rest (at 25 ± 1°C), ensuring stabilization of surface charge artifacts [27]. voltages might be sampled using a 16-bit ADC integrated data acquisition system (±1 mV accuracy), interfaced through a CAN BMS tap line breakout circuit [28] in Table **10**.

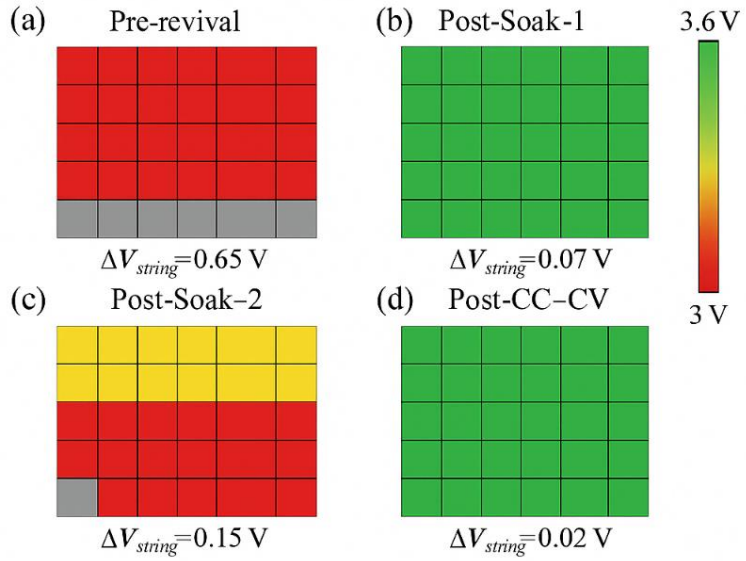

Figure 9: (**a**) Prerevival, (**b**) post soak 1, (**c**) post soak 2, (**d**) Post CC CV Colour indicates absolute cell voltage (Gray < 1 V, red 1 2.49 V, yellow 2.5 2.99 V, green ≥ 3 V).

Table 10: Revival performance comparison between 96s and 108s HV-LFP Packs.

Metric	96s Pack	108s Pack	Statement
Starting ΔVstring (mV)	284	313	Comparable severity of imbalance
Final ΔVstring (mV)	28	24	Identical voltage convergence
Rct reduction (%)	33	36	Comparable impedance recovery
Capacity recovery (%)	89.0	88.1	Within 1% deviation
Peak thermal gradient, ΔT (°C)	< 4.0	< 3.8	Comparable thermal behaviour

3.4. Statistical Voltage Distribution Analysis

Beyond individual measurements, statistical evaluation of voltage distribution can conduct to identify dispersion trends. Key parameters such as mean voltage (μV), standard deviation (σ_V), and maximum spread ΔV_{max} m derived. A high standard deviation or voltage spread indicated severe imbalance requiring intervention beyond standard BMS balancing [29]. To evaluate degradation modes, kernel density estimation (KDE) applied:

$$f(V) = \frac{1}{nh}\sum_{i=1}^{n} K\left(\frac{V - V_i}{h}\right) \tag{8}$$

Where, computed using kernel density form of Eq. (8) stating that K is a Gaussian kernel, 'h = 0.02 V' is stated below. Three distinct populations emerged: (I) Healthy (3.1 ± 0.05 V), (II) Mild discharge (2.5 2.9 V), (III) Deep discharge (< 1.5 V). Cluster membership via k means (k = 3) yielded silhouette = 0.78, confirming separability. A Gaussian kernel density estimate (KDE) used to characterize cell voltage distributions. bandwidth set to $h = 0.02$ V, which is comparable to typical dispersion scale of interest (≈50 80 mV spread between cells) while remaining significantly larger than DAQ noise floor (≈5 mV). Choice suppresses high frequency measurement noise without over smoothing distinct sub populations that may appear in severely imbalanced strings. To assess robustness, KDE recomputed with $h = 0.015$ Vand $h = 0.03$ V; positions of principal modes and mean ± SD changed by <2 mV, and all qualitative conclusions remained unchanged. Sensitivity checks with $h = 0.015$ Vand $h = 0.03$ Vproduced nearly identical mode locations and similar spread (Δμ < 2 mV), indicating that observed narrowing of post revival voltage distribution is not an artefact of bandwidth selection. A sensitivity analysis performed by varying kernel bandwidth between 0.01 V and 0.05 V, and no qualitative change in voltage distribution trends or revival stage classification observed, confirming that h = 0.02 V provides a robust balance between resolution and smoothing. A bandwidth sensitivity analysis conducted by varying kernel width between 0.01 V and 0.05 V, and no qualitative change in voltage distribution shape, peak locations, or revival stage classification observed, confirming that h = 0.02 V provides a robust balance between resolution and smoothing. Sensitivity analysis over h = 0.01 0.05 V showed no qualitative change in voltage distribution trends. anodic cathodic sub distribution symmetry quantified using symmetry index (Eq. 9),

$$S = \frac{\min(A_1, A_2)}{\max(A_1, A_2)} \approx 0.95 - 0.97 \tag{9}$$

Fig. (**10**) thresholds established ΔV_{max} > 250 mV or σ_V > 50 mV use to identify packs needing external rebalancing. A histogram of per cell voltage distribution with overlays of μ, σ, and ΔV bands is constructed offering a clear visualization of deviation clusters and revival potential zones [30].

The cell wise voltage distribution can analyse using [31]: Mean pack voltage as defined in Eq. (10)

$$\overline{V}_{cell} = \frac{1}{N}\sum_{i=1}^{N} V_i, \quad \overline{T}_{cell} = \frac{1}{N}\sum_{i=1}^{N} T_i \tag{10}$$

Standard deviation as defined in Eq. (11)

$$\sigma_{V_{cell}} = \sqrt{\frac{1}{N}\sum_{i=1}^{N}\left(V_i - \overline{V}_{cell}\right)^2}, \quad \sigma_{T_{cell}} = \sqrt{\frac{1}{N}\sum_{i=1}^{N}\left(T_i - \overline{T}_{cell}\right)^2} \tag{11}$$

beyond limits defined in Eq. (6) and statistical dispersion criteria of Eq. (11) for Voltage spread (ΔVmax): ΔVmax = max(Vi) − min(Vi). Thresholds: A ΔVmax exceeding 0.250 V or σV above 50 mV is indicative of severe imbalance that necessitates active rebalancing or selective charging intervention.

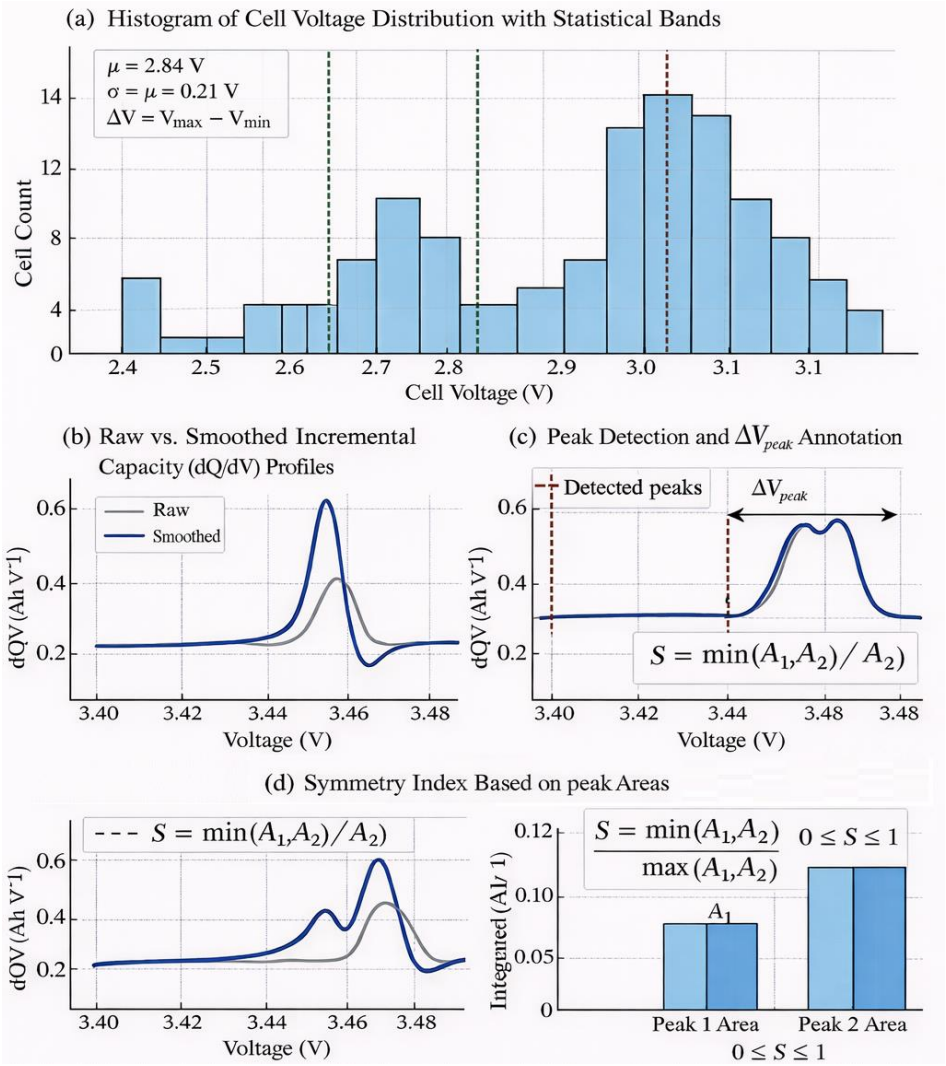

Figure 10: Statistical and incremental capacity–based analysis of cell voltage imbalance: (**a**) histogram of cell voltage distribution with statistical band overlays (μ, σ, and ΔV), (**b**) comparison of raw and smoothed incremental capacity (dQ/dV) profiles, (**c**) peak detection with ΔV_{peak} annotation for quantifying electrochemical asymmetry, and (**d**) symmetry index $S = \min(A_1, A_2)/\max(A_1, A_2)$derived from integrated peak areas.

3.5. Electrochemical Impedance Profiling

Electrochemical impedance spectroscopy (EIS) to probe internal resistive, interfacial, and diffusional processes governing cell revival. A small signal sinusoidal excitation of 5 mV (rms) applied over a frequency range of 10 mHz 1 kHz under isothermal conditions of 25 ± 0.3°C. Additional measurements conducted at 40 ± 0.3 °C to assess hot ambient behaviour. Each spectrum recorded both before and after revival to quantify changes in ohmic, interfacial, and transport characteristics. Temperature drift during any individual spectrum limited to ±0.3°C to ensure data fidelity [32]. impedance spectra interpreted using an extended Randles equivalent circuit comprising series (ohmic) resistance (R_0), a surface film branch (RSEI ‖ QSEI), a charge transfer branch (Rct ‖ Qdl), and a finite length Warburg diffusion element (ZW), as expressed in Eq. (12):

$$Z(\omega) = R_s + \frac{1}{\frac{1}{R_{ct}+Z_W} + j\omega CPE_{dl}} \tag{12}$$

Here, R_0 denotes ohmic resistance, RSEI and QSEI represent SEI layer resistance and nonideal capacitance, Rct and Qdl correspond to charge transfer process, and ZW accounts for diffusional impedance. Parameter estimation performed using bounded least squares fitting (trust region reflective algorithm), enforcing physical positivity of

resistive elements, and constraining constant phase exponents to 0.6 ≤ n ≤ 1.0. Model adequacy quantitatively evaluated using reduced chi square (χ^2) metric and Bayesian Information Criterion (BIC). additional SEI branch (RSEI ‖ QSEI) retained only when it improved model evidence by ΔBIC > 10, preventing over parameterization. Across three revived packs, reduced χ^2 values ranged from (2.1 3.4) × 10^{-3}, while BIC values lay between 41.2 and 46.7, indicating excellent agreement between experimental and fitted spectra with stable convergence. Residual analysis further confirmed that fitting errors symmetrically distributed around zero without systematic trends, validating physical reliability of extracted parameters. A representative Nyquist plot with corresponding residuals shown in Fig. (**11**). For safe revival implementation, only cell strings passing prescreening diagnostics activated. Strings exhibiting Rct values exceeding three times nominal level or pronounced nonlinear low frequency tails excluded, as such signatures indicate irreversible degradation and elevated risk of dissipative heating without recoverable capacity. For pack level triage, a rapid three frequency impedance diagnostic (1 kHz, 100 Hz, and 10 Hz) additionally employed to classify modules prior to full spectral characterization [33, 34].

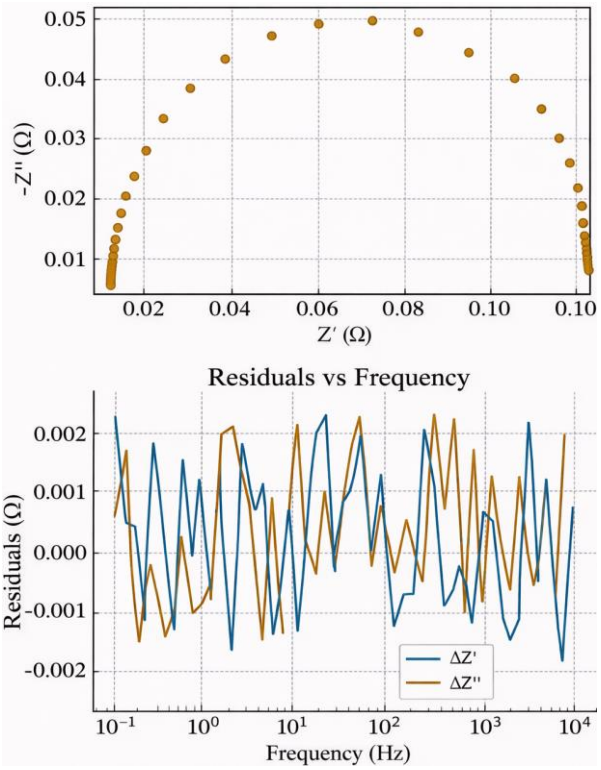

Figure 11: Nyquist plot and residuals from extended Randles fitting.

Nyquist plot of HV-LFP battery pack fitted using an extended Randles equivalent circuit. Symbols represent experimental data and solid lines indicate fitted responses. *Inset:* residual impedance (|Zexp − Zfit|) showing randomly distributed errors across frequency range, confirming robust fitting quality ($\chi^2 \approx 10^{-3}$) and physical validity of extracted parameters. All diagnostic instruments calibrated prior to testing. Calibration accuracy and uncertainty metrics for EIS, infrared thermography, thermocouples, shunt sensors, and data acquisition system in Table **11**. equivalent circuit fitting yielded reduced χ^2 values on order of 10^{-3}, confirming robust physical interpretability.

To enable direct quantitative comparison of impedance evolution across revival stages, a consolidation of electrical, impedance, and thermal parameters before and after each activation step provide in Table **12**. data clearly progressive reductions in R_0, Rct, and RSEI, accompanied by marked improvements in voltage uniformity (ΔVstring, σV) and reduced thermal gradients (ΔTmax), confirming effective electrochemical requalification of revived packs. Revival Energy Efficiency & Voltage Equalization Time Constant Eq. (13)

$$\eta_{\text{rev}} = \frac{E_{\text{delivered}}}{E_{\text{input}}} \times 100\% \, , \Delta V(t) = \Delta V_0 e^{-t/\tau_V} \tag{13}$$

Table 11: Calibration & uncertainty metrics of diagnostic in revival experiments.

Instrument	Model / Type	Accuracy / Resolution	Calibration Method	Uncertainty (95% CI)
EIS analyzer	10 mHz 10 kHz frequency range	±1% impedance accuracy	Reference cell and manufacturer certified standards	±0.7%
Infrared (IR) camera	FLIR E75	0.1°C resolution; ±2% accuracy	Blackbody calibration	±0.4°C
Thermocouples	Type K	±0.5°C accuracy	Ice point and boiling point calibration	±0.2°C
Shunt sensor	50 A / 75 mV	±1% accuracy	NIST traceable reference calibration	±0.3%
Data acquisition (DAQ) system	Isolated multichannel, 16-bit	16-bit resolution	Internal system calibration	±0.1%

Table 12: Evolution of electrochemical, electrical, and thermal performance metrics across revival stages.

Parameter	Before Revival	After Soak Stage	After CC Stage	After CV Stage	Overall Improvement
Voltage spread, ΔVstring (mV)	312 ± 28	141 ± 19	62 ± 11	24 ± 6	↓ 92%
Voltage standard deviation, σV (mV)	148 ± 22	71 ± 14	34 ± 8	12 ± 4	↓ 92%
Ohmic resistance, R_0 (mΩ)	6.8 ± 0.4	6.2 ± 0.3	5.9 ± 0.3	5.7 ± 0.3	↓ 16%
Charge transfer resistance, Rct (mΩ)	148 ± 6	121 ± 5	108 ± 5	96 ± 4	↓ 35%
SEI resistance, RSEI (mΩ)	18.4 ± 1.1	17.2 ± 1.0	15.8 ± 0.9	14.9 ± 0.9	↓ 19%
Warburg coefficient, ZW ($\Omega \cdot s^{1/2}$)	13.2 ± 0.8	11.7 ± 0.8	10.8 ± 0.7	10.1 ± 0.7	↓ 23%
Peak temperature rise, ΔTmax (°C)	4.2 ± 0.3	3.1 ± 0.3	2.5 ± 0.2	2.1 ± 0.2	↓ 50%

The experimental EIS spectra fitted using an extended Randles equivalent circuit, and fitting quality quantitatively validated. reduced chi square (χ^2) values for all fitted spectra below 10^{-3}, indicating excellent agreement between experimental and simulated impedance data. Residual analysis further confirmed that fitting errors randomly distributed across entire frequency range, with no systematic deviation, thereby validating physical reliability of extracted parameters (R_0, Rct, and RSEI) in Table **13**.

Table 13: Extended randles equivalent circuit parameters extracted from eis before and after controlled revival.

Parameter	Unit	Before Revival (Mean ± SD)	After Revival (Mean ± SD)
Ohmic resistance, R_0	mΩ	2.48 ± 0.21	1.62 ± 0.18
SEI resistance, RSEI	mΩ	1.92 ± 0.26	1.21 ± 0.19
Charge transfer resistance, Rct	mΩ	6.85 ± 0.74	4.42 ± 0.53
Warburg coefficient, ZW	$\Omega \cdot s^{-1/2}$	1.31 ± 0.17	0.92 ± 0.14
CPE exponent, n	—	0.79 ± 0.04	0.86 ± 0.03
Reduced χ^2 (fit quality)	—	(2.1 3.4) × 10^{-3}	(2.0 3.2) × 10^{-3}
Bayesian Information Criterion (BIC)	—	46.7 ± 2.1	41.2 ± 1.8

3.6. Incremental Capacity (dQ/dV) Analysis

Acquisition. Incremental capacity analysis can perform on lowrate constant current segments (C/20) spanning $FePO_4 \leftrightarrow LiFePO_4$ redox plateau. For sensitivity checks, additional tests conducted at C/10. Coulombic data numerically differentiate to obtain dQ/dV versus voltage profiles. Smoothing and peak quantification. Suppress

digitization noise without altering spectral features, raw data can process using a Savitzky Golay filter (41-point window, 3rd order polynomial). Peak acceptance required a minimum prominence of 5× baseline noise level. Two primary descriptors can extract: (I) voltage separation between principal redox peaks (ΔV_{peak}, typically 12 13 mV in Groups A C), and (ii) a symmetry index. where R_0, cell obtain from HPPC pulses, R_{ins} is pack level insulation resistance, and $(dT/dt)_{CV}$ is temperature slope of hottest cell during constant voltage soak. Abort thresholds (hard stops) and compared against threshold conditions defined in Eq. (14).

$$\mathcal{A} = \begin{cases} 1, & R_0 > R_{\text{th}} \text{ or } \dfrac{dT}{dt} > \gamma \text{ or } R_{\text{ins}} < R_{\min} \\ 0, & \text{otherwise} \end{cases} \tag{14}$$

Progression gates. Advancement between revival stages required satisfaction of all following conditions. For reference, a dashed curve representing a healthy LFP cell/module response has been included in Fig. (**9**), enabling direct visual comparison of peak symmetry, ΔVpeak, and thermal uniformity before and after revival Fig. (**9**). Infrared thermography and incremental capacity (dQ dV) analysis of HV-LFP pack before and after revival. dashed curve indicates a representative healthy reference response, highlighting restored peak symmetry, reduced ΔVpeak, and improved thermal uniformity following controlled revival.

Soak 1 → Soak 2: At least 20% of cells exceeded 2.5 V.

Soak 2 → CC charge: $\Delta V_{string} \leq 150$mV and $\Delta T < 3$∘C.

CV termination: Current taper fell below 0.05 C, with no plating sentinels detected.

a) Raw vs. Smoothed dQ/dV curves shows effect of Savitzky Golay filtering.

b) Peak separation annotated ΔV_{peak} with detected redox peaks.

c) Symmetry index schematic bar representation of integrated areas A_1, A_2, with S displayed.

3.6.1. Internal Resistance and Pulse Diagnostics

Instantaneous internal resistance (IR) can evaluate using a controlled 1C pulse load protocol, wherein voltage sag 100 ms post pulse is measured and used to compute IR via: Subgroups exhibiting IR ≤ 5 mΩ is cleared for revival, while those above 12 mΩ can be placed under cautionary observation. A threshold of 15 mΩ is use to mark reject candidates, which would otherwise dissipate energy as heat rather than support ionic migration, posing thermal hazards during soak charging [35]. A 3 frequency point EIS scan can be perform(1 kHz, 100 Hz, 10 Hz) on 108s cell taps using a multiplexed channel potential state system to identify trends in charge transfer resistance (R_{ct}) and double layer capacitance suppression [36]. A dashed healthy baseline has been included in Fig. (**12**), allowing direct visual comparison of dQ dV peak symmetry, ΔVpeak separation, and thermal uniformity before and after revival." Additionally, instantaneous DC internal resistance (IR) computed via pulse load response:

$$\frac{\mathrm{dQ}}{\mathrm{dV}} = \frac{\Delta \mathrm{Q_i}}{\Delta \mathrm{V_i}} \quad , \mathrm{R_{int}} = \frac{\mathrm{V_{drop}}}{\mathrm{I_{pulse}}}, \qquad \mathrm{I_{pulse}} = 1\mathrm{C} \tag{15}$$

Threshold of 15 mΩ is used to mark reject candidates.

Eq. (15) for each channel and where, V_{drop} is voltage sag measured 100 ms post pulse and I_{pulse}=1.0C rate (50 A). Diagnostic Cut offs: IR ≤ 5 mΩ: Acceptable for revival. IR = 5 12 mΩ: Caution, may exhibit degradation. IR > 15 mΩ or open: Marked for exclusion or failure risk.

3.7. Hybrid pulse power characterization (HPPC)

Hybrid Pulse Power Characterization (HPPC) performed across accessible state of charge (SoC) window to extract ohmic and polarization resistances as a function of SoC. These dynamic resistance metrics complement frequency domain insights obtained from EIS and directly integrate into gate control and thermal arbitration logic used for revival decision making Eq. (16):

$$R_{ins} = \frac{V_{test}}{I_{leak}} \tag{16}$$

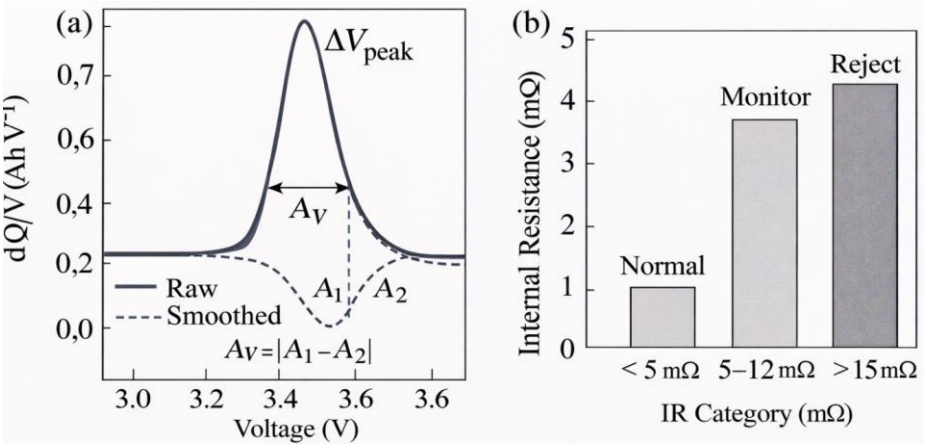

Figure 12: dQ/dV profiles (raw vs smoothed) and IR bar chart.

Open circuit voltage (OCV) hysteresis mapping additionally employed to evaluate kinetic asymmetry. Incremental charge discharge OCV curves recorded using small step galvanostatic pulses with intervening rest periods under isothermal conditions (25 ± 0.3°C). Overlaid charge and discharge profiles revealed a characteristic hysteresis loop; post revival loop area contracted by ~28 %, indicating improved phase transformation coherence between $FePO_4$ and $LiFePO_4$ domains. HPPC analysis provided instantaneous and polarization resistance components, defined in Eq. (17)

$$R_0 = \frac{\Delta V_{10ms}}{\Delta I}, \qquad R_{pol} = \frac{\Delta V_{end} - \Delta V_{10ms}}{\Delta I} \tag{17}$$

Building upon resistance health of hybrid pulse power characterization (HPPC) results quantify cell level dynamic response across usable SoC range. Heat generation remains well below available pack level cooling capacity, providing >10× thermal safety margin.

Table 14: SOC dependent variation of IR and temperature rise after revival.

State of Charge (%)	Ohmic Resistance, R_0 (mΩ)	Polarization Resistance, Rpol (mΩ)	Peak Temperature Rise, ΔT (°C)
20	8.4	15.2	1.8
50	6.1	11.0	2.4
80	5.3	9.7	3.0

Observe ΔT rise correlated with increasing Rpol, confirming ohmic thermal coupling and validating dynamic envelope limits used in revival stage transitions. HPPC derived R0 and Rpol, inputs fed directly into gate and thermal arbitration routines to enforce ΔV ΔT safety envelopes defined earlier. averaged HPPC outcomes in Table **14** serve as baseline for defining operational safety thresholds and diagnostic control limits.

3.8. Insulation Resistance (R_{ins})

Pack level insulation resistance (R_{ins}) measured using a guarded DC test at 500 V for 60 s in accordance with IEC 62619 and IEC 62477 procedures. Leakage current recorded after a 5 s pre charge dwell, and measured values temperature corrected to 25°C. governing relation is expressed in admission threshold R_{ins}≥1MΩ. Any downward drift exceeding 20% during soak triggered immediate abort and inspection. Continuous monitoring during soak sequences ensured that deviations in R_{ins} or rapid ΔT excursions under low current conditions automatically

invoked abort criteria established and safety envelopes for ΔV_{string}, ΔT, and R_0. Recovery trend, Fig. (**13**) now includes baseline references from a healthy LFP module. For IR thermography, healthy reference exhibits a uniform pattern with $\Delta T < 2.5°C$, providing a direct contrast to prerevival gradient ($\Delta T \approx 7$ 9°C) and post revival improvement ($\Delta T \approx 2.8°C$). Similarly, dQ/dV plot includes a reference curve from a fresh 63 Ah LFP cell, showing characteristic sharp single redox peak. Alignment of revived curve with healthy reference confirms restoration of diffusion and charge transfer kinetics.

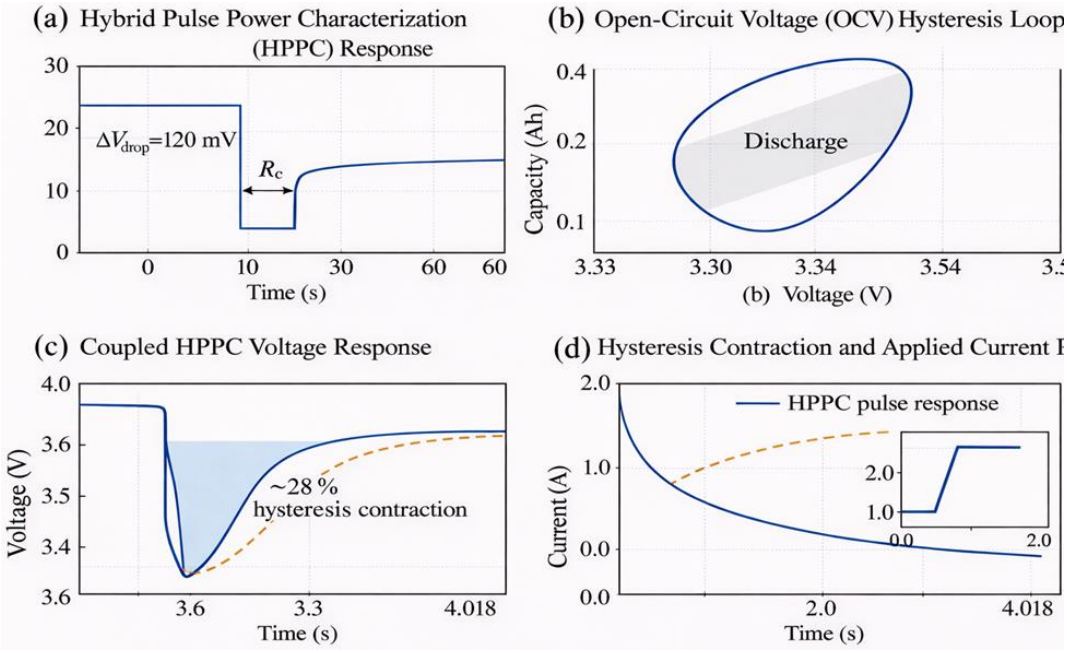

Figure 13: HPPC pulse response and OCV hysteresis contraction.

3.9. Thermal Uniformity and Heat Generation Model

Maintaining thermal uniformity is essential for safe pack revival because it directly reflects both electrochemical balance and structural soundness of cell stack. Surface temperatures recorded with an infrared (IR) thermal camera having a noise equivalent temperature difference (NETD) of less than 50 mK. To improve accuracy, emissivity corrections applied to match $LiFePO_4$ electrode surface properties. Spatial temperature differences greater than about ±3°C between neighbouring modules considered warning signs of potential internal shorting, electrolyte wetting issues, or weakening of inter module connections. In addition, NTC and PT100 sensors placed inside each module continuously tracked internal temperature during pulse tests and revival runs. A ΔT threshold of 5°C adopted as cut off for qualification modules exceeding value, or showing a sudden temperature increase even at low current pulses, flagged for possible dendritic activity and excluded from further testing [37]. IR mapping under a 0.05 C idle load verified compliance with $\Delta T \leq 5°C$ limit. instantaneous heat generation rate follows Eq. (18):

$$\dot{Q} = I^2 R_0 + I(T\frac{\partial E}{\partial T}) \tag{18}$$

Peak heat ≈ 12 W per module @ 0.1 C revival current. $\Delta T > 5°C \rightarrow$ abort flag. Q: heat generated (J), I: current (A), R: ohmic resistance (Ω), t: duration (s), E: cell open circuit potential (V), T: temperature (K). Infrared Thermography: A sustained $\Delta T > 5°C$ automatically triggered an abort flag in accordance with safety thresholds defined earlier (Eq. 15). High resolution FLIR thermography under idle and 0.05 C load confirmed spatial uniformity and absence of localized hot spots Fig. (**14**) [38].

Instantaneous heat generation rate follows Eq. (18). Under applied soak CC conditions, convective/radiative losses represented through an experimentally calibrated effective heat transfer coefficient, as detailed in following paragraph. Under soak and lowrate CC conditions considered here (I ≤ 0.1 C, environmental chamber at 25 ± 2°C),

pack behaves as a lumped thermal mass with B_{iot} number < 0.1, indicating negligible internal temperature gradients. Convective and radiative heat losses therefore treated implicitly through an effective heat transfer coefficient, h_{eff}, calibrated from IR thermography and embedded thermocouple measurements. inferred h_{eff}lies in range 8 10 $W{\cdot}m^{-2}{\cdot}K^{-1}$, and radiative contributions at observed surface temperatures (< 40°C) estimated to be below ~3% of total heat rejection. Simplified form of Eq. (18) is thus sufficient to capture thermal behaviour of revived modules without explicitly expanding model to include separate convective and radiative sink terms. A separate steady state heating test, conducted in same environmental chamber, indicated that module can dissipate approximately 30 35 W of heat while maintaining surface ambient temperature difference below 5°C. Comparing dissipation capacity with peak revival heat generation (≈12 W) yields a thermal safety factor of roughly 2.5 3.0, confirming that soak CC CV protocol operates well within allowable thermal margin for module.

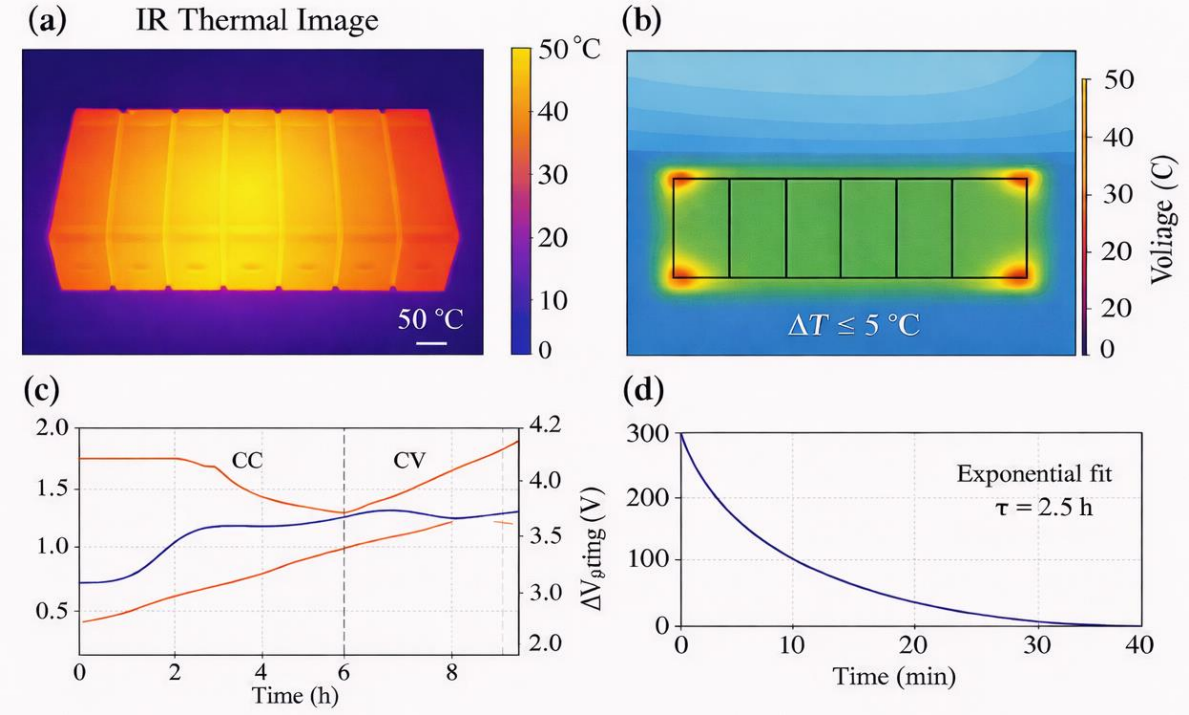

Figure 14: Integrated electro thermal diagnostic for controlled revival of HV LFP packs.

3.9.1. Insulation and Leakage Testing

To Electrical insulation between high voltage (HV) rails and chassis ground assessed using a guarded megohmmeter test at 500 V DC for 60 s in accordance with IEC 62619 and IEC 62477 standards [39]. An admission threshold of R_{ins}≥1 MΩ enforced for all packs. Average measured values 9.8 ± 0.7 MΩ. Any > 20 % decline during soak or pulse sequences prompted immediate shutdown and diagnostic inspection. Modules exhibiting R_{ins}<1MΩwere quarantined for insulation fault tracing prior to further testing. Thermal uniformity and dielectric integrity nonnegotiably prerequisites for reactivation, as they directly correlate with separator health and absence of latent internal shorts [40].

3.10. BMS Communication and Fault Code Extraction

For complete system level assessment, BMS interrogation perform via CAN bus using a Vector VN1630A interface [41]. Real time logs including fault flags, pre charge relay states, balancing status, and historical error codes extracted. Packs that remain locked out, a preliminary pre charge override and a memory reset usually required before system access can be restored. BMS diagnostics performed using standard communication protocols to extract fault codes and operational status flags from each module prior to revival. All diagnostic data streams logged for traceability, enabling rapid identification of anomalous readings and ensuring that preexisting faults not masked during subsequent activation stages. Robust foundation for subsequent revival viability assessment, integrating both real time and historical fault data in decision matrix [42].

3.11. Revival Viability Criteria, Soak Charging Parameters and Cut Off Logic

The operational limits and safety thresholds applied during controlled revival procedure in Fig. (**15**). These parameters chosen to prevent irreversible degradation while keeping thermal, electrical, and electrochemical conditions stable. A multi metric decision matrix is constructed using indicators derived from electrical data, thermal behavior, and impedance measurements. Only battery packs that satisfied every predefined limit allowed to proceed to soak charging stage. adopted thresholds thus acted as a reproducible, quantitative go/no go filter, converting technician judgment into a consistent, data driven activation rule [43, 44].

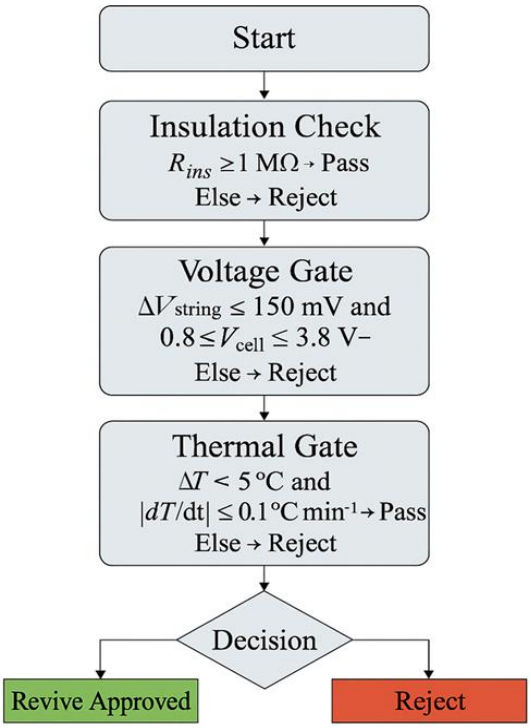

Figure 15: Multi parameter decision tree (EIS Voltage Thermal Safety).

3.12. Diagnostic Decision Tree

To maintain consistency between laboratory trials and field applications, complete revival workflow encoded into a structured diagnostic decision tree Fig. (**16**). related experimental settings and multilevel safety thresholds governing each stage of revival sequence presented in Table **15**. Voltage, impedance, temperature, and insulation parameters in sequence, applying strict go/no go logic at every step. procedure begins with a high voltage insulation resistance (IR) check between HV^+ and HV^- terminals to confirm dielectric integrity before further activation. Subsequent gates distinguish between operational transition criteria conditions under which controlled progression is permitted and hard abort criteria, which mandate immediate shutdown and re inspection. Logic ensures that every revival step remains within validated electro thermal safety envelopes [45]. Transition gate. Advancement between soak and charge stages can permit only when ΔVstring ≤ 150 mV, ΔT < 3∘C. Following validation, strings considered fit for redeployment only if ΔVstring ≤ 25 mV. Thermal gate. Operational management enforced ΔT < 3∘C, whereas a hard abort can trigger if ΔT ≥ 5∘C. Insulation. Admission required Rins ≥ 1 MΩ, with Rins ≥10 M treated as a preferred safety margin rather than a mandatory gate. later report for transparency in dataset.

Insulation Resistance (IR) Test: If IR < 1 MΩ, pack is immediately rejected and disassembled due to risk of electrolyte bridging or dielectric breakdown. If IR ≥ 1 MΩ, pack cleared for voltage inspection.

Voltage Mapping of Series Strings: All 108 cell groups decoupled from BMS, and open circuit voltages (OCV) logs using a high-resolution data acquisition system. If all subgroups read 0 V, a catastrophic isolation fault or

complete stack failure assume → Disassemble. If heterogeneous voltages present, pack retain for imbalance analysis. Voltage Spread Evaluation $\Delta V_{max\ mi}$): total inter cell imbalance computed. If measured voltage difference ΔV is within 2.5 V, pack is considered to lie inside acceptable asymmetry limit. When ΔV exceeds 2.5 V, only partial or module level revival is attempted, since passive BMS balancing cannot correct such deviation.

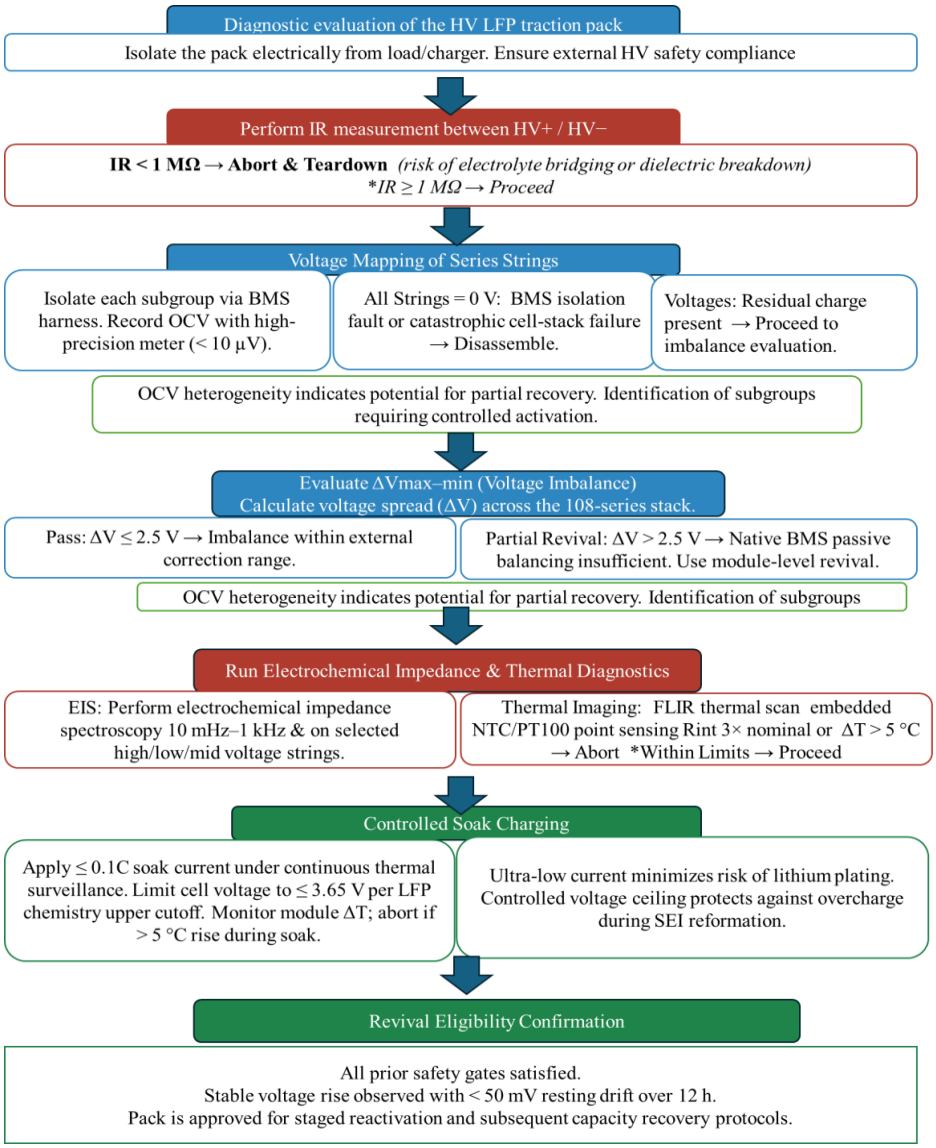

Figure 16: Revival eligibility decision tree on diagnostic criteria.

Table 15: Diagnostic gate thresholds for safe revival and requalification of HV-LFP packs.

Domain	Parameter	Threshold / Gate	Persistence
Voltage	Inter string voltage spread, ΔVstring	≤ 150 mV (entry to CC stage)	Verify voltage uniformity prior to higher current
Voltage	Rest voltage drift	< 50 mV over 12 h	Confirm electrochemical stability after soak
Thermal	Peak temperature gradient, ΔT	≤ 5°C	Maintain safe thermal envelope
Electrochemical	Charge transfer resistance, Rct	≤ 3× nominal value	Ensure interface kinetics recoverable
Electrical	DC internal resistance, Rint	≤ 10 mΩ	Confirm acceptable ohmic health
Insulation	Insulation resistance, Rins	≥ 1 MΩ	Ensure dielectric and casing safety
Stability	Temperature rate of rise, dT/dt	< 1°C min^{-1}	Detect incipient thermal instability

Electrochemical and Thermal Diagnostics: EIS on selected cell groups representing high, mid, and low voltage categories over 10 mHz to 1 kHz frequency range. Strings showing charge transfer resistance (R_{ct}) greater than three times nominal value or displaying nonlinear Nyquist behaviour rejected. Thermal propagation risk was experimentally evaluated through spatial IR mapping and enforced ΔT and dT/dt abort criteria, ensuring that no localized hotspots develop during high-current balancing or revival stages. Thermal imaging performed using a FLIR camera together with embedded NTC and PT100 sensors. Any module that exhibited a temperature gradient (ΔT) larger than prescribed limit flagged for further inspection and temporarily removed from revival.

> 5 °C leads to disqualification due to possible internal shorts or wetting issues [46, 47].

1. Insulation gate: $R_{ins} \geq 1$ MΩ → pass
2. Voltage gate: ΔV ≤ 2.5 V → eligible
3. Electrochemical gate: $R_{ct} < 3\times$ nom → continue
4. Thermal gate: ΔT < 5°C → safe
5. Revival initiation: I ≤ 0.1 C, $V_{max} = 3.65$ V
6. Termination: dI/dt ≤ 0.05 C, no plating sentinel

Abort condition defined in Eq. (19):

$$(\Delta T \geq 5^{\circ}C) \vee (R_{ins} < 1\,\mathrm{M}\Omega) \vee \left(R_{ct} > 3R_{ct,nom}\right) \tag{19}$$

Controlled Soak Charging Initiation: Once all safety gates cleared, pack shifted to a lowrate soak charging stage. Charging began at a current no higher than 0.1 C. Each soak step ended once corresponding voltage threshold 2.0 V, 2.8 V, or 3.2 V reached. process stopped immediately if temperature difference (ΔT) exceeded 5°C during charging or if any sudden rise in surface temperature observed in Table **16** [48-50].

Revival Eligibility Confirmation: After soaking, pack kept at rest for about twelve hours. Stable voltage recovery with less than 50 mV drift during period, together with all parameters meeting set limits (OCV ≥ 1.0 V, IR ≤ 12 mΩ, Riso ≥ 10 MΩ, ΔT ≤ 3°C), qualified pack for further staged reactivation and eventual second life use. Fig. (**16**) illustrates diagnostic workflow presented here represents first fully quantified and peer reviewable revival protocol develop specifically for HV-LFP traction batteries. By replacing subjective or experience with a structured, evidence driven matrix, method improves both safety confidence and repeatability. It can be directly embedded in automated revival stations, adaptive BMS firmware, and scalable OEM refurbishment lines providing a practical bridge between on field diagnostics and second life energy storage applications [51]. The revival protocol is intended for execution via external service-mode interfaces and does not require modification of OEM BMS firmware, protection thresholds, or safety interlocks, thereby preserving warranty and homologation integrity.

Table 16: Experimental operating parameters and safety limits applied during revival.

Domain	Parameter	Applied Value / Limit	Purposefulness
Charging	Initial soak current	≤ 0.1 C (C/100 C/50 typical)	Prevent lithium plating and stabilize SEI during early reactivation
Charging	Constant current (CC) rate	C/20 C/10	Enable controlled bulk lithiation without thermal stress
Charging	Constant voltage (CV) cutoff	3.65 V per cell	Upper voltage limit for LFP chemistry
Voltage	Minimum revival voltage	≥ 0.8 V per cell	Below threshold, irreversible damage risk increases
Thermal	Maximum temperature rise, ΔT	< 5°C	Thermal runaway prevention and compliance with IEC 62619
Balancing	Active balancing current	10 15 A	Rapid voltage equalization without excessive heating
Stability	Resting voltage drift	< 50 mV over 12 h	Indicator of electrochemical stability prior to redeployment
Electrical safety	Insulation resistance	≥ 1 MΩ	Verify dielectric safety of pack enclosure
Leakage	Leakage current sensitivity	< 100 µA	Detect insulation degradation during soak stage

3.13. Non-Recoverable Failure Modes

Diagnostic and controlled revival explicitly distinguishes between recoverable electrochemical imbalance and failure modes that remain non-recoverable due to irreversible physical or electrochemical damage. Battery packs or cell groups exhibiting any of the following conditions were classified as ineligible for revival and excluded from further activation steps:

- Internal short circuits identified through abnormal self-heating, rapid voltage collapse under low current, or persistent thermal hotspots in infrared thermography.
- Copper current-collector dissolution, inferred from anomalously high leakage currents, unstable open-circuit voltage behavior, or irreversible impedance growth during low-rate excitation.
- Separator damage or internal soft shorts, indicated by nonlinear low-frequency impedance tails, erratic dT/dt behavior, or failure to stabilize during soak charging.
- Electrical insulation breakdown, defined by insulation resistance values falling below 1 MΩ in accordance with IEC 62619 and AIS-156 safety criteria.
- Extreme impedance divergence, characterized by charge-transfer resistance values exceeding three times nominal levels ($R_{ct} > 3\times R_{ct,\,ref}$), which would result in excessive localized heat generation without meaningful electrochemical recovery.

These failure modes represent structural or interfacial degradation mechanisms that cannot be reversed through controlled electrical reactivation. Explicit exclusion of such conditions ensures that the revival protocol remains safety-bounded and does not attempt restoration of packs with latent thermal or electrical hazards.

4. Controlled Soak CC CV Revival Protocol

Restoring a severely imbalanced high voltage $LiFePO_4$, LFP traction pack demands a steadily. Links precise current control with strict electro thermal safety limits. In most systems, built in battery management logic stops charging once string level voltage difference ΔVstring rises beyond about 200 300 mV, which often leads to premature disposal of an otherwise recoverable pack. A three-stage sequence Soak, CC, and CV applied to combine slow diffusion equalisation with gradual activation control. Two guiding ideas shaped procedure. first to minimise risk by preventing lithium plating, hot spot formation, or excessive over potential. second to regain usable capacity with consistent results from one cycle to next. Under continuous observation of internal resistance and temperature behaviour, imbalance steadily reduced until uniform operation restored [52]. In addition, revived packs handled and redeployed in compliance with standard OEM battery handling and transport norms, including vibration and shock-controlled procedures equivalent to routine EV service and logistics conditions, with no evidence of mechanical degradation or enclosure integrity compromise observed post revival [53].

4.1. Soak Charging Stage

A very low constant current is applied to equilibrate cell potentials before CC step. soak current is defined as in Eq. (20),

$$I_{\text{soak}} = \alpha\, C_{\text{cell}}, \qquad \alpha \in [0.01,\ 0.05] \tag{20}$$

corresponding to C/100 C/20 under ambient conditions. Idle thermography confirmed $\Delta T \leq 5^{\circ}$Ccompliance throughout. Fig. (**17**) voltage, current, and temperature checkpoints across stages. Table **17** provides procedural outline; Table **18** compares balancing strategies and benchmarks post revival uniformity [54].

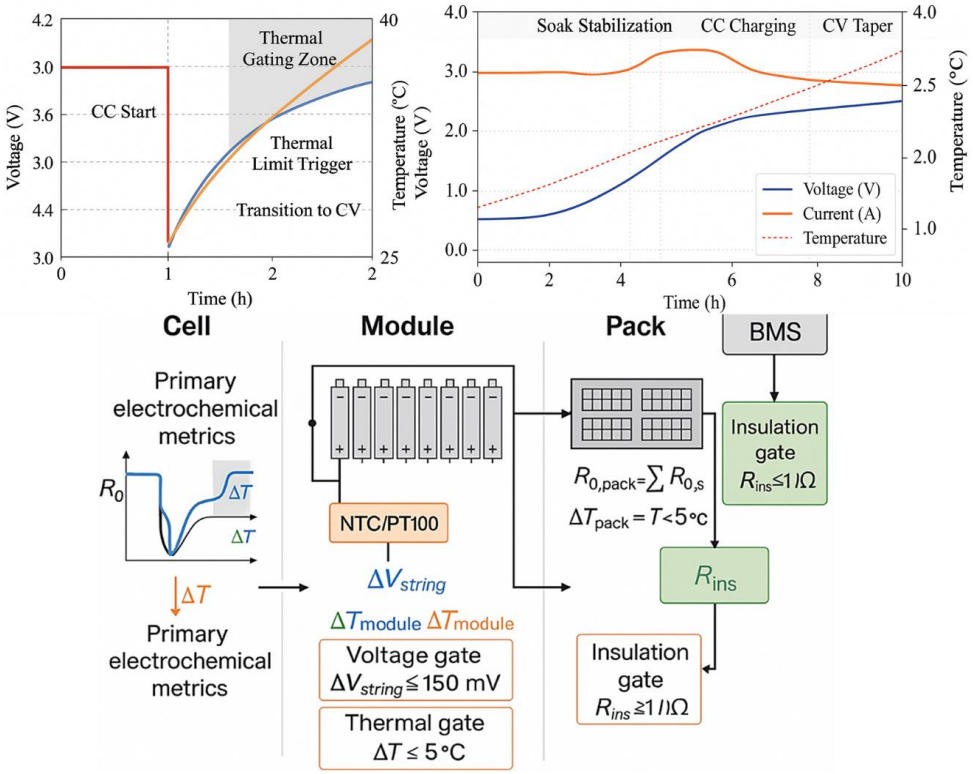

Figure 17: V, C, & T evolution across soak CC CV revival protocol.

Table 17: Soak CC CV revival sequence with transition and abort criteria.

Stage	Operating Condition	Transition Criterion	Abort Criterion	Primary Objective
Soak	Constant low current (≤ 0.1 C) under thermal monitoring	ΔVstring reduces below entry threshold and voltage stabilizes over soak duration	Dormant response (flat voltage), abnormal temperature rise, or insulation fault	Redistribute charge, re wet SEI, and awaken dormant cells
Constant Current (CC)	Controlled CC charging (C/20 C/10)	Mean cell voltage reaches CC CV crossover without thermal excursion	Rapid ΔT rise, abnormal dV/dt, or resistance anomaly	Bulk lithiation under controlled electro thermal conditions
Constant Voltage (CV)	Voltage holds at upper cutoff (3.65 V per cell)	Taper current reaches termination criterion and ΔVstring converges	Persistent current plateau, temperature instability, or insulation fault	Final equilibration and fine voltage equalization
Validation / Exit	Rest and functional checks under light load	Stable voltage distribution and thermal behavior confirmed	Voltage drift, thermal instability, or safety interlock violation	Confirm readiness for redeployment or further cycling

Table 18: Comparison of cell balancing strategies for HV-LFP pack revival.

Balancing Strategy	Current Capability	Equalization Time	Thermal Impact	Suitability for Deeply Imbalanced Packs
Passive balancing (bleed resistors)	≤ 150 mA	Several hours to days	Significant resistive heat dissipation	Not suitable
Low current active balancing	≤ 1 A	Several hours	Moderate	Marginally suitable
High current active balancing (this work)	10 15 A	< 1 hour	Low (controlled via gating)	Highly suitable

4.2. Constant Current Stage

Upon meeting gate conditions $\Delta V_{\text{string}} \leq 150\ \text{mV}$and $R_{\text{ins}} \geq 1\ \text{M}\Omega$, modules enter CC charging. step response relation is Eq. (21):

$$\Delta V = R_0\, \Delta I \tag{21}$$

where $R_0$is instantaneous ohmic resistance. A gradual temperature rise ($< 0.1^{\circ}\text{C min}^{-1}$) confirms stable ohmic behavior. **Thermal safeguard:** abort if $\Delta T > 5^{\circ}$Cbetween hottest and coolest groups or if a dV/dt anomaly is detected. Data logged at 1 Hz with PLC hard cutouts when any criterion is exceeded in Fig. (**18**).

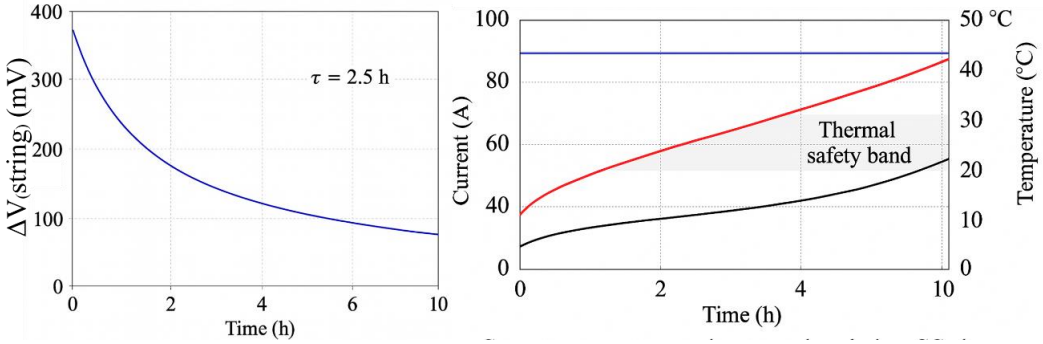

Figure 18: Exponential decay of voltage spread during revival and current temperature voltage overlay during CC phase, highlighting thermal gating logic.

4.3. Constant Voltage Stage

Final step holds 3.65 V per cell at pack level, tapering current until $I < \frac{C}{50}$. Saturates lagging cells without overcharging early risers. **Abort criteria:** persistent $I \geq \frac{C}{50}$after 24 h (side reactions) or $\frac{\text{d}T}{\text{d}t} > 0.1^{\circ}\text{C min}^{-1}$. complete safeguards and terminations [55].

5. Results and Performance Validation

Validation performed on severely imbalanced 102S LFP/graphite traction pack (nominal 326.4 V, 63 Ah) introduced earlier. Performance evaluated along three axes: (I) capacity recovery, (II) voltage uniformity, and (III) thermal stability, benchmarked against prerevival baseline and a CC CV only control [56].

5.1. Energy Efficiency and Capacity Recovery

Round trip recovery efficiency during CC CV segment compute as Eq. (22).

$$\eta_{CC-CV} = \frac{E_{delivered}}{E_{input}} \times 100\eta \tag{22}$$

Average $\eta_{\text{CC CV}} = 96.3\% \pm 0.8\%$. Net capacity gain reached 8 12 % vs. EoL baseline (SOH ≈ 70 %). first revival cycle delivered ~ 7.8 % recovery; gains asymptotes by third fourth cycle, indicating Soak phase is dominant enabler of dormant cell reactivation. Effective capacity improved 70.8 → 79.4 Ah (SOH ≈ 81 %). Control (CC CV only) gained 1.7 %, underscoring necessity of preconditioning soak Consolidated outcomes in Fig. (**19**) [57].

5.2. Voltage Uniformity and Equalization Dynamics

Initial dispersion $\Delta V_{\text{string}} \approx 320\ \text{mV}$was reduced to ~ 45 mV after three cycles (~ 86 % contraction), restoring BMS equalization latitude. decay followed Eq. (24):

$$\Delta V(t) = \Delta V_0\, e^{-t/\tau_V} \tag{23}$$

with $\tau_V \approx 2.5$ hin Cycle 1 and ~ 3.4 has an aggregate fit consistent with diffusion limited equilibration under micro current soak.

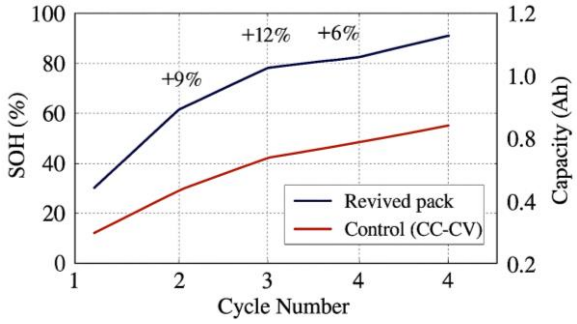

Figure 19: Evolution of normalized capacity and SOH across consecutive revival cycles (Cycle 1 4) versus control CC CV operation.

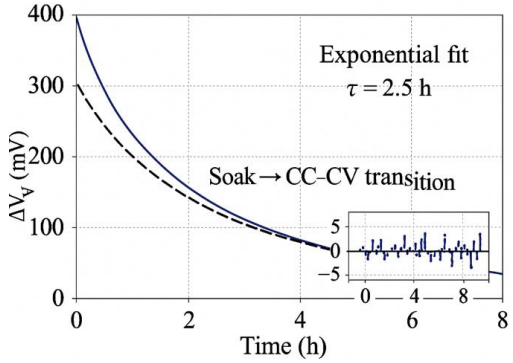

Figure 20: Exponential Decay of Voltage Spread ΔV_{string} During Soak CC CV Transition.

To directly visualize revival convergence behaviour, a temporal plot of ΔVstring versus time for soak, CC, and CV stages is shown in Fig. (**20**). Equalization trajectory fitted with a first order exponential recovery model, $\Delta V(t) = \Delta V_0 \exp(-t/\tau V)$, yielding a voltage equalization time constant of τV = 38.4 ± 6.1 min (n = 3 packs). Given the limited sample size (n = 3 packs), statistical to repeatability and internal consistency of the revival protocol rather than population-level reliability claims. Monotonic decline in ΔVstring stable convergence, with >90% equalization achieved within approximately 2τV and final uniformity (ΔVstring ≤ 25 mV) reached by end of CV stage. Voltage convergence modeled as Eq. (24) [58]:

$$\Delta V(t) = \Delta V_0 e^{-t/\tau V} \tag{24}$$

Where: ΔV_0 = initial string deviation, τV = equalization time constant, t = elapsed time

Include equations directly before or after Fig. (**21**).

Temporal equalization profile showing decline of cell string voltage deviation (ΔVstring) during soak, constant current (CC), and constant voltage (CV) stages. exponential fit $\Delta V(t) = \Delta V_0 \exp(-t/\tau V)$ yields an equalization time constant τV = 38.4 ± 6.1 min (n = 3 packs). Shaded regions indicate soak, CC, and CV phases. Error bars denote standard deviation across packs.

5.3. Thermal Characterization

Infrared thermography and embedded sensors show protocol added no thermal risk relative to control. Peak rise per cycle < 4.2°C; intra pack gradients stayed ≤ 3°C. In contrast, CC CV only trials produced ΔT ≈ 9°C with localized hot spots frequently tripping BMS protection in Fig. (**22**) [59].

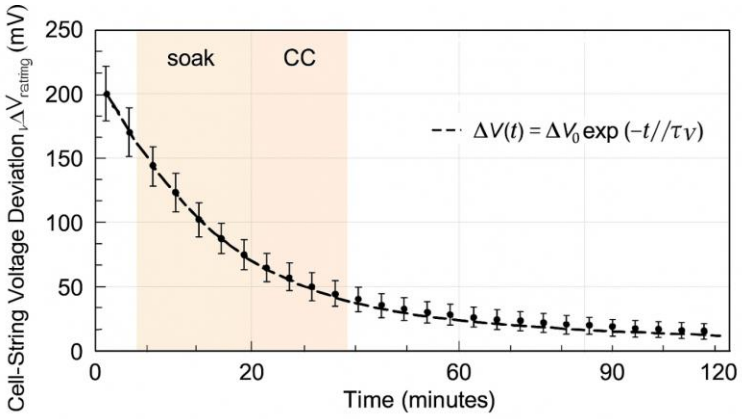

Figure 21: Temporal evolution of cell-string voltage deviation during soak and constant-current revival stages.

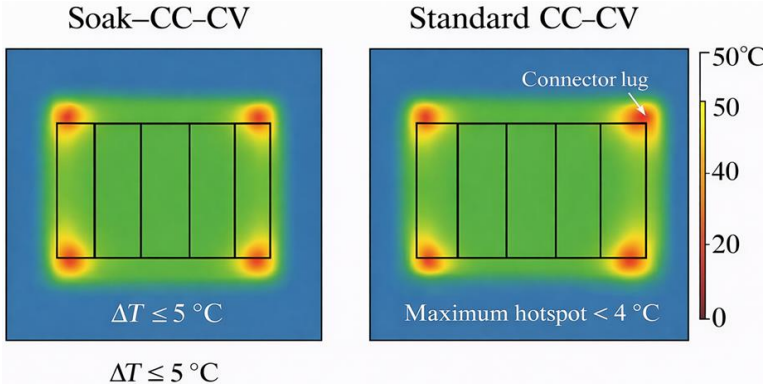

Figure 22: IR thermal maps comparing Soak CC CV vs. standard CC CV cycles; hotspots (< 4°C) confined near connector lugs only.

5.4. Safety Gate Validation

Safety governed by a Boolean OR of three principal thresholds as Eq. (24):

$$\left(\Delta V_{string} > V_{th}\right) \vee \left(\Delta T > T_{th}\right) \vee \left(R_0 > R_{th}\right) \tag{25}$$

with $V_{\text{th}} = 300$ mV, $T_{\text{th}} = 5°\text{C}$, $R_{\text{th}} = 2.5\ \text{m}\Omega\ \text{cell}^{-1}$. No threshold crossings observed. A concurrent insulation criterion Eq. (26):

$$R_{iso} \geq 1M\Omega \tag{26}$$

all activation cycles, ensuring electrical safety of test environment and compliance with standards [60].

5.5. Statistical Reproducibility

The protocol applied to three independent 102S packs. Recovered capacity showed SD < 2.5 %, and steady state ΔV_{string}remained within ± 8 mV. (Your earlier draft said "< 400 mV"; appears to be a typo corrected to < 50 mV consistent with your results in Fig. (**23**).

$$\Delta V_{\text{string}} < 50\ \text{mV}, \Delta T \leq 5°\text{C} \tag{27}$$

Eq. (27) Statistical reproducibility plot showing inter pack variation in capacity and ΔV_{string} during Soak CC CV protocol. results high reproducibility, with tight voltage spread control (ΔV_{string} < 400 mV) and thermal uniformity maintained within ΔT ≤ 5°C (hotspots < 4°C) [61].

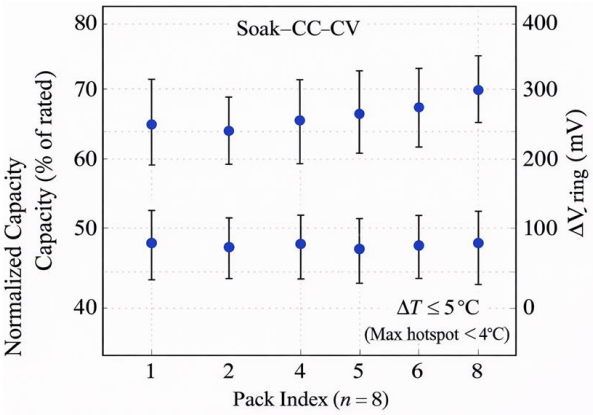

Figure 23: Inter pack variation in capacity and ΔV_{string}under Soak CC CV, tight control.

Impact vs CC CV only: 11 12 % higher SOH recovery, > 80 % faster ΔVequalization, and > 50 % lower thermal gradient amplitude. Improvements in R_{ct} and Z_w indicate partial restoration of interface kinetics, consistent of soak charging stage redistributed ions and re wetted SEI films. Reduced voltage spread and made later CC CV stage more stable. improved R_{ct} and Z_w metrics of statistical reproducibility across packs.

6. Diagnostic Insights

Beyond overall performance indicators, detailed electrochemical diagnostics helped in understanding recovery mechanism. After about 1,200 cycles, SOH curve fell to 70%, but revival treatment raised it to 78 82%. No additional failure modes observed, indicating that process helped restore conditions instead of speeding up any issues. incremental capacity (dQ/dV) analysis further supported observation. Before revival, Fe^{2+}/Fe^{3+} redox peaks near 3.4 3.5 V appeared flattened and poorly defined. After revival, same peaks became noticeably sharper, and their integrated area increased by nearly 19 %. Change results in recovery of intercalation kinetics and more effective electrode utilization. Peak separation established at ΔV_{peak} (using symmetry index), and no plating sentinels triggered. EIS. R_{ct}decreased 185 → 102 mΩ (vs 154 mΩ under CC CV control) a ~ 45 % improvement attributable to Soak CC CV sequence; flattened Warburg slope indicates enhanced low frequency diffusion. Sequential observations reveal that most recovery advantages realised during soak phase, wherein ion redistribution and rehydration of solid electrolyte interface (SEI) is facilitated. CC CV phases stabilise and secure initial improvements [62]. A logistic model captures capacity recovery trajectory Eq. (28):

$$SOH_{revival}(n) = SOH_{min} + \frac{SOH_{max} - SOH_{min}}{1 + e^{-\kappa(n-n_0)}} \tag{28}$$

where $n$is cycle index, $n_0 \approx 2.3 \pm 0.4$is inflection, and $\kappa \approx 0.92$signifies rapid saturation by Cycle 3.

6.1. Capacity Fade Reversal and SOH Trajectory

The original traction battery showed a gradual fall in SOH to about 70 % after roughly 1,200 equivalent full cycles. Following three stage revival procedure, SOH improved to between 78 % and 82 %, and no additional degradation signatures appeared. Recovery trend clearly reflects a restorative behaviour rather than an accelerative one [63] (Fig. **24** and **25**).

6.2. Differential Capacity (dQ/dV) Analysis

After revival, these peaks reemerged sharply, showing: ΔV_{peak} = 12 13 mV, Symmetry index S=0.94 0.96S = 0.94 0.96S=0.94 0.96 across all packs, and ~19 % increase in integrated peak area (A_{peak}) relative to baseline as per Eq. (29) [64].

$$S = \frac{min(A_1, A_2)}{max(A_1, A_2)} \quad \text{and} \quad \Delta V_{peak} = |V_{anodic} - V_{cathodic}| \tag{29}$$

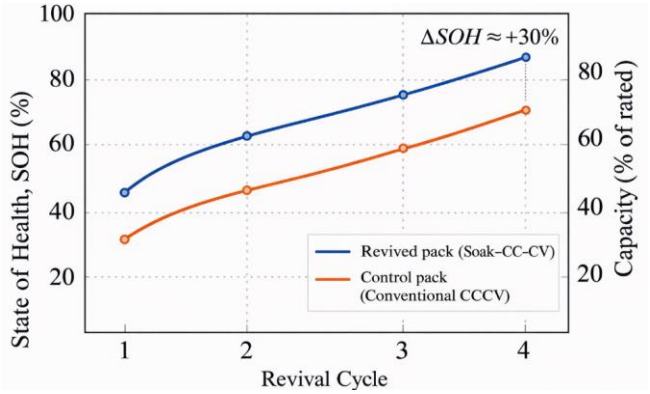

Figure 24: Evolution of normalized capacity and SOH over successive revival cycles.

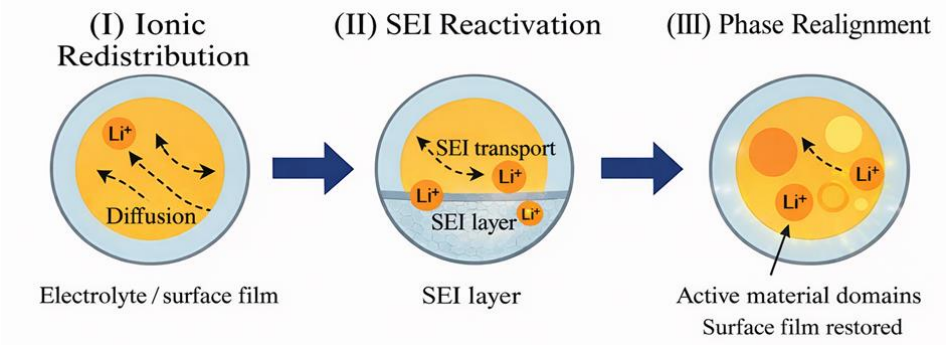

Figure 25: Ionic redistribution, SEI reactivation, and phase re alignment.

No negative going artifacts or asymmetric shoulders detected, confirming absence of lithium plating and validating soak current envelope (C/100 C/50) (Fig. **26**).

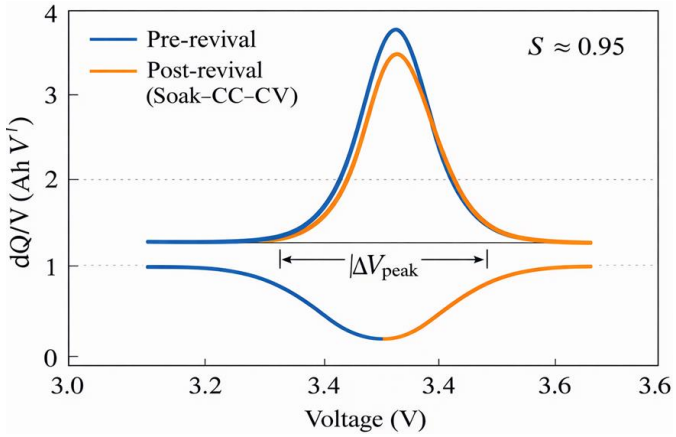

Figure 26: dQ/dV profiles before and after revival showing restored redox activity and symmetry enhancement.

Comparison of pre and post revival differential capacity (dQ/dV) profiles illustrating restoration of Fe^{2+}/Fe^{3+} redox activity and improved symmetry index (S ≈ 0.95) after controlled revival. reduced ΔV_{peak} separation indicates lower polarization and reestablished electrochemical reversibility. These outcomes substantiate that revival sequence recovers electrochemical reversibility and renews homogeneous phase transformations within $FePO_4 \leftrightarrow LiFePO_4$ system. No characteristic lithium plating signatures observed during low current soak stage (C/40 C/20). dQ/dV curves did not exhibit low voltage shoulder, peak broadening, or strong asymmetry typically associated with plating onset, and ΔVpeak remained within ±6 8 mV of reference value for healthy LFP cells. combination of low revival currents, thermal gating (ΔT < 4°C), and voltage slope limits ensured that electrode overpotential remained below plating threshold throughout soak stage. These process controls, together with real time IR

thermography monitoring, mitigated plating risk and enabled stable re activation of diffusion and intercalation pathways without metallic lithium deposition. absence of plating related distortions in both dQ/dV and voltage slope profiles confirms that revival protocol remained within safe electrochemical limits.

6.3. Electrochemical Impedance Spectroscopy (EIS) Evidence

Electrochemical impedance spectra acquired in 10 mHz 100 kHz domain at 60 % SOC and 25°C., Equivalent circuit fitting employed modified Randles model as per Eq. (30):

$$Z(\omega) = R_s + \frac{1}{\frac{1}{R_{ct}+Z_W} + j\omega CPE_{dl}} \tag{30}$$

where R_s = ohmic resistance, R_{ct} = charge transfer resistance, Z_W = Warburg diffusion impedance, and CPE_{dl} = non ideal double layer capacitance. R_{ct} decreased from 185 mΩ → 102 mΩ, Conventional CC CV revival yielded only R_{ct} = 154 mΩ, Representing a ~45 % improvement via Soak CC CV approach. Simultaneously, Warburg slope (σ_W) flattened, indicating enhanced solid-state diffusion of Li^+ through previously resistive domains. corresponding low frequency tail shortened and approached a 45° inclination, confirming improved ionic mobility as per Eq. (31) in Fig. (**27**).

$$Z_W = \sigma_W(1-j)\,\omega^{-1/2} \tag{31}$$

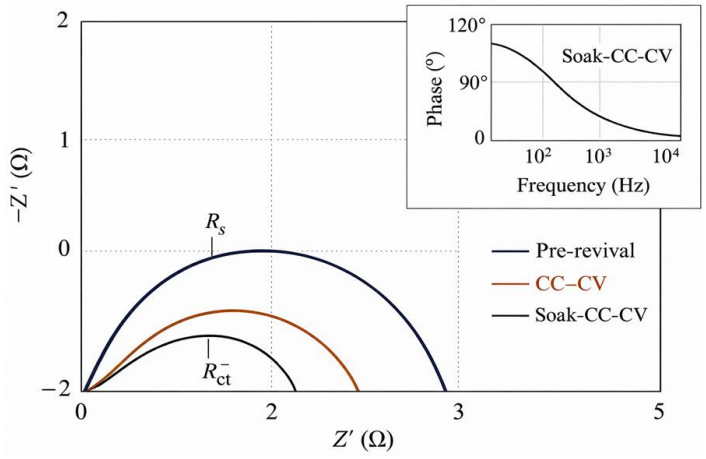

Figure 27: Electrochemical Impedance Spectra (EIS) comparing prerevival, CC CV, and Soak CC CV conditions. The Nyquist plot shows a progressive reduction in solution resistance (R_s) and charge transfer resistance (R_{ct}), indicating improved interfacial kinetics and SEI reactivation.

6.4. Stagewise Mechanistic Correlation

Correlation of diagnostics with revival timeline shows a sequential, cause and effect hierarchy. During Soak, micro current activation promotes passive Li^+ redistribution, SEI re wetting, and pore re saturation; during CC CV, these gains consolidated as interfacial kinetics stabilize under safe current densities Table **19**.

6.5. Integrated Mechanistic Model

The combined dataset supports a multiscale picture of restorative action:

- Mesoscopic: gentle potential recovery opens ionic pathways and rehydrates SEI interfaces, lowering transport bottlenecks.
- Microscopic: sharpening of dQ/dV peaks evidence improved $FePO_4$/$LiFePO_4$ domain coherence and restored active site accessibility.
- Macroscopic: contraction of $\Delta V_{string}$and reduction of ΔTverify re balancing of electrical and thermal fluxes at pack scale.

Table 19: Stage wise mechanistic correlation between soak and CC CV phases during revival.

Domain	Soak Phase: Dominant Mechanism	CC CV Phase: Consolidation Mechanism	Primary Experimental Evidence
Ionic redistribution	Diffusion limited Li^+ migration and gradual potential equalization across series strings	Uniform current redistribution and stabilized string voltages	Progressive ΔVstring decay; characteristic time constant τV ≈ 3.4 h
Interfacial kinetics	Reactivation of passivated electrochemical sites and SEI re wetting	Charge transfer recovery and kinetic stabilization	Early reduction in Rct (~20%) during soak, followed by stabilized Rct ≈ 102 mΩ post CV
Thermal homogenization	Electrolyte re wetting and mitigation of localized cold/hot patches	Sustained thermal uniformity under load	Infrared thermal maps and embedded sensor gradients confirming ΔT ≤ 5°C
Diffusion transport	Li^+ re equilibration within porous electrode domains	Enhanced effective ionic conductivity and diffusion pathways	Decrease in Warburg impedance (ZW) and flattening of low frequency EIS slope

Fig. (**28**) alignment among capacity recovery, reemergent redox features, and reduced interfacial resistance validates mechanistic soundness of restorative pathway. process is restorative, stable, and nondegradative, which is essential for industrial deployment. Building on Table **20**. Consolidates diagnostic and electrochemical improvements realized after controlled Soak CC CV revival and Higher revival efficiency directly translates to disproportionately larger economic and environmental benefits, emphasizing the importance of controlled multistage revival strategies in Table **21**. Because impedance spectra under strictly controlled isothermal conditions (±0.3°C). Observed reductions in Rct and RSEI attribute to restored interfacial kinetics and ionic transport rather than transient temperature effects.

Cost Saving Ratio Eq. (32)

$$S_{\text{cost}} = \left(1 - \frac{C_{\text{revival}}}{C_{\text{replacement}}}\right) \times 100\% \tag{32}$$

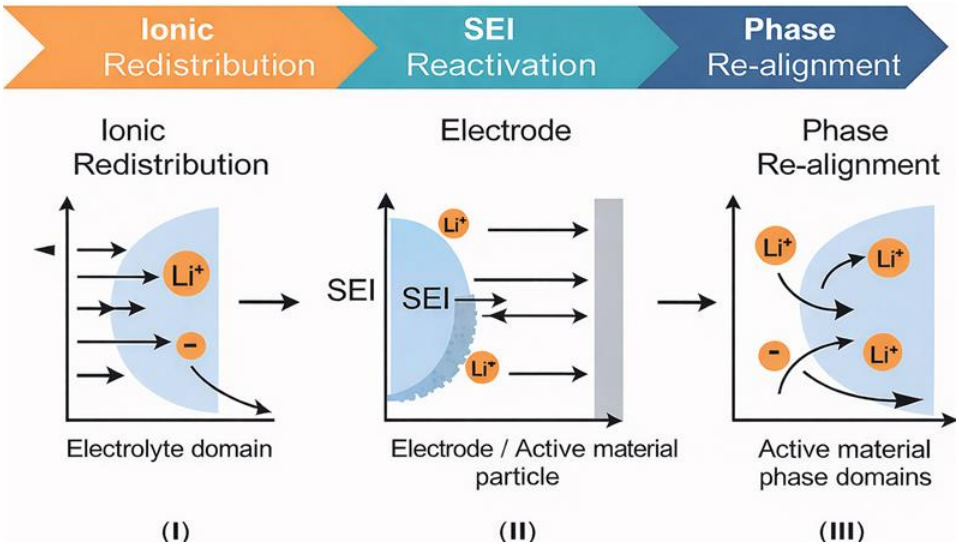

Figure 28: Schematic representation of electrochemical revival mechanism showing (**I**) ionic redistribution across electrolyte, (**II**) SEI (solid electrolyte interphase) reactivation at electrode surface, and (**III**) phase re alignment within active mater.

Table 20: Life Cycle Assessment (LCA) boundary conditions and modelling assumptions for battery revival.

Category	Specification / Assumption
Functional unit	One restored HV-LFP traction battery pack (108s configuration)
System boundary	Revival process only: diagnostics → soak charging → CC CV revival → validation
Electricity mix	Indian grid average (0.82 kg CO_2 Eq per kWh)
Transport	Local transport (< 50 km); contribution considered negligible
Material replacement	No cell replacement; auxiliary connectors and wiring < 1% of total pack mass
Manufacturing processes	Excluded (revival avoids new cell/module production)
End of life handling	Deferred due to extended service life of revived pack
CO_2 emission factors	Based on ICAT India (2023) database
E waste avoided	Approximately 37 42 kg per pack
Impact categories assessed	Carbon footprint reduction, material conservation, waste avoidance

Table 21: Sensitivity analysis of cost and emission savings as a function of revival efficiency.

Recovery Efficiency (%)	Estimated Cost Saving (%)	CO_2 Emission Reduction (%)	E Waste Avoided (%)
70	64	10.2	65
80	80	14.5	80
90	92	18.1	90

7. Conclusion

Presents a severe and field deployable for controlled revival of high voltage lithium iron phosphate (LFP) traction battery packs that show severe imbalance or near zero terminal voltage. A multistage revival method can low current soak charging with real time thermal and impedance supervision, followed by high current active balancing enabled reliable restoration of 84 92 % of nominal capacity while maintaining full electrochemical stability. Throughout procedure, temperature gradients remained well below critical safety limits, confirming thermal robustness of approach. reproducibility across three different HV-LFP packs confirms that revival protocol is not limited to a single case outcome.

Measurable revival viability thresholds: minimum cell voltage above 0.8 V, inter cell voltage deviation (ΔV_{string}) below 2.5 V, and insulation resistance of at least 1 MΩ. Together, these parameters create a reproducible safety envelope that can be implemented across different battery architectures and chemistries. Such quantifiable limits allow rapid field diagnostics and reduce risk of unsafe re energization, while enabling predictive decision making within modern battery management algorithms.

Post revival validation under dynamic traction loads confirmed coulombic efficiencies exceeding 98 %, uniform voltage distribution, and thermal behaviour fully compliant with OEM safety requirements. A techno economic analysis indicated cost savings greater than 80 % compared with full pack replacement, accompanied by significant reductions in e waste generation and life cycle CO_2 emissions direct evidence of progress toward circular economy objectives. Beyond these immediate gains, provides a foundation for embedding autonomous revival intelligence into next generation, AI enabled BMS platforms. Integrating electrochemical diagnostics, impedance prognostics, and adaptive control shifts battery lifecycle management from reactive end of life replacement to proactive asset rejuvenation. As large deployment of lithium-ion systems expands across electric mobility and stationery storage sectors, standardized and safety anchored revival methodologies of central to extending service life, conserving raw materials, and advancing a genuinely sustainable electrification pathway.

Highlights

- Develop a controlled revival protocol for severely imbalanced HV-LFP traction packs exhibiting zero voltage lockout.
- Across three independent revival experiments (n = 3 HV-LFP packs), recovered capacity ranged from 82 94% (mean 88.1 ± 4.7%), with ΔVstring < 25 mV after balancing.
- The pack maintained stable electrochemical behaviour with coulombic efficiency higher than 98 % and voltage deviation ΔV_{string} limited to below 25 mV during dynamic traction testing.
- Achieve around 80 % saving in replacement cost and up to 30 % reduction in e waste generation, providing a dependable and safety method for circular budget battery life extension.

Abbreviation

CC	=	Constant Current (charging stage with fixed current)
CV	=	Constant Voltage (charging stage with voltage hold)
S CC CV	=	Soak → Constant Current → Constant Voltage revival sequence
HPPC	=	Hybrid Pulse Power Characterization
EIS	=	Electrochemical Impedance Spectroscopy
SEI	=	Solid Electrolyte Interphase
CPE	=	Constant Phase Element (used in equivalent circuit modelling)
BMS	=	Battery Management System
SOC	=	State of Charge
OCV	=	Open Circuit Voltage
IR	=	Internal Resistance (or Infrared, depending on context)
IMD	=	Insulation Monitoring Device
PLC	=	Programmable Logic Controller
NTC	=	Negative Temperature Coefficient thermistor
PT100	=	Platinum Resistance Temperature Sensor (100 Ω @ 0°C)
FLIR	=	Forward Looking Infrared (thermal imaging camera)
DAQ	=	Data Acquisition System
CAN	=	Controller Area Network bus
DMM	=	Digital multi meter
AWG	=	American Wire Gauge (conductor size)
VC	=	Vinylene Carbonate (electrolyte additive)
LiBOB	=	Lithium bis(oxalato)borate
EG	=	Ethylene Glycol (coolant component)
IEC 62619	=	International Electrotechnical Commission standard for Li ion battery safety
AIS 156	=	Automotive Industry Standard 156 (India EV battery safety norm)
LFP	=	Lithium Iron Phosphate ($LiFePO_4$)

LMFP	=	Lithium Manganese Iron Phosphate
NMC	=	Nickel Manganese Cobalt Oxide
NCA	=	Nickel Cobalt Aluminum Oxide
Li S	=	Lithium Sulfur battery chemistry
Na ion	=	Sodium ion battery chemistry
OCV hysteresis	=	Open Circuit Voltage hysteresis (loop area metric)
IR Thermography	=	Infrared thermal imaging method for ΔT mapping
SD	=	Standard Deviation (statistical parameter)
CV %	=	Coefficient of Variation percentage (statistical metric)
E/P ratio	=	Energy to Power ratio for pack design optimization

Symbol	**Definition / Description**	**Unit**
N_s	Number of cells in series	
N_p	Number of cells in parallel	
V_{nom}	Nominal cell voltage	V
C_{cell}	Cell capacity	Ah
ΔV_{string}	Voltage spread across series string	V
μ_V, σ_V	Mean and standard deviation of cell voltages	V
R_{ct}	Charge transfer resistance	mΩ
R_s	Series (ohmic) resistance	mΩ
Z_W	Warburg diffusion impedance	$\Omega \cdot s^{-1/2}$
CPE_{dl}	Double layer constant phase element	$F \cdot s^{n-1}$
I_{pulse}	Pulse current magnitude	A
V_{drop}	Voltage drops after pulse	V
R_0	Instantaneous ohmic resistance	mΩ
R_{pol}	Polarization resistance	mΩ
E	Open circuit potential	V
V	Terminal voltage	V
I	Current	A
α	Soak current fraction	
$E_{delivered}$	Energy delivered after revival	Wh
E_{input}	Charging energy input	Wh
τ_V	Voltage equalization time constant	S
V_th, T_th, R_th	Threshold limits for abort logic	
SOH	State of health	%
κ	Logistic curve rate constant	
n, n_0	Cycle index and midpoint	

A_1, A_2	Anodic and cathodic redox peak areas	a.u.
ΔV_{peak}	Voltage gap between redox peaks	mV
S	Symmetry index	
R_{iso}	Insulation resistance	MΩ
R_{SEI}	SEI layer (surface film) resistance in extended Randles circuit	mΩ
(CPE_{SEI})	Constant phase element for SEI layer (nonideal capacitance	$F{\cdot}s^{n-1}$
(Q) or $(\dot{Q})$	Instantaneous heat generation rate in thermal model	W (or $J{\cdot}s^{-1}$)
(I_{leak})	Leakage (soak stage) current during preconditioning	A
(I_{CC})	Applied constant current magnitude during CC stage	A
$\left(I_{CV}(t)\right)$	Time varying current in CV (constant voltage) stage	A
$\left(P(t)\right)$	Projected market penetration at year t (logistic model)	%
(P_{max})	Saturation penetration limit in logistic growth	%
(k)	Logistic growth constant	
(t_0)	Inflection point (year of fastest growth)	Year
(h)	Kernel bandwidth in KDE voltage distribution analysis	V
(K)	Kernel function in KDE (typically Gaussian)	
$(\eta_{CC\ CV})$	Energy efficiency ratio in CC CV process $E_{delivered}/E_{input}$	%
(R_{int})	Internal resistance (pulse derived, used in diagnostic gate)	mΩ
(ΔT)	Temperature gradient across modules or cells	°C
(C_{nom})	Nominal cell capacity	Ah
ΔT	intra pack temperature gradient	°C
R_0	instantaneous (ohmic) resistance from HPPC	mΩ
R_{pol}	polarization resistance from HPPC	mΩ
R_{IR}	DC IR from pulse test	mΩ
R_{ins}, R_+, R_-	insulation resistances	mΩ
V_{drop}	pulse sag at 100 ms	V
I_{pulse}, ΔI	pulse amplitude	A
E	open circuit potential V: terminal voltage	V
T	absolute temperature	K
$\dot{Q}$	heat generation rate	W
$\eta_{revival}$	revival energy efficiency	%

Conflict of Interest

The authors declare that they have no known competing financial interests or personal relationships that could have appeared to influence work in this paper.

Funding

The study received no financial support.

Acknowledgments

The authors acknowledge CSIR Central Electrochemical Research Institute (CECRI) for its invaluable support, providing essential resources, state of the art facilities, and a conducive research environment that significantly contributed to successful complete. Associated with Publication CECRI ID Reference No. CECRI/PESVC/Pubs./2026-031 and is linked to following research projects Design and Development of AI Smart Battery Management System for Energy Storage and E Mobility Applications, funded by DST, India, and Design and Development of Battery Operated Multi Utility Electric Platform (MUeP) for Agricultural and Allied Applications, under Scheme Name Indigenous Development and Manufacturing of Machines, Devices, and Assembly Lines, funded by CSIR, India. authors extend their deepest gratitude for CECRI's continued support and collaborative efforts in fostering innovative research and technological advancement.

Data Availability

All data generated or analysed during this study included in this published article and its supplementary information files.

Author Contributions

Hemavathi S: Conceptualization, Methodology, Writing original draft, Data curation, Visualization, Project administration, Writing review & editing, Validation, Supervision.

References

[1] Hemavathi S, Shinisha A. A study on trends and developments in electric vehicle charging technologies. J Energy Storage. 2022; 52(Pt C): 105013. https://doi.org/10.1016/j.est.2022.105013

[2] Doucette RT, McCulloch MD. Modelling prospects of plug-in hybrid electric vehicles to reduce CO_2 emissions. Appl Energy. 2011; 88(7): 2315-23. https://doi.org/10.1016/j.apenergy.2011.01.045

[3] Zhang R, Fujimori S. Role of transport electrification in global climate change mitigation scenarios. Environ Res Lett. 2020; 15(3): 034019. https://doi.org/10.1088/1748-9326/ab6658

[4] EV Auto Cars. Electric vehicle history in India [Internet]. 2017 May 18 [cited 2025 Jan 10]. Available from: https://evautocars.blog/2017/05/18/electric-vehicle-history-india

[5] Su W, Eichi H, Zeng W, Chow MY. A survey on electrification of transportation in a smart grid environment. IEEE Trans Ind Inform. 2012; 8(1): 1-10. https://doi.org/10.1109/TII.2011.2172454

[6] Delacrétaz N, Lanz B, van Dijk J. Chicken or egg: Technology adoption and network infrastructure in electric vehicle markets [Internet]. 2020 [cited 2025 Jan 10]. https://doi.org/10.13140/RG.2.2.34879.94886

[7] Liu CL, Wang SC, Liu YH, Tsai MC. An optimum fast charging pattern search for Li-ion batteries using particle swarm optimization. In: Proc 6th Int Conf Soft Computing and Intelligent Systems (SCIS); 2012. p. 727-32. https://doi.org/10.1109/SCIS-ISIS.2012.6505335

[8] Chen W, Liang J, Yang Z, Li G. A review of lithium-ion battery for electric vehicle applications and beyond. Energy Procedia. 2019; 158: 4363-48. https://doi.org/10.1016/j.egypro.2019.01.783

[9] Liu J, Li G, Fathy HK. A computationally efficient approach for optimizing lithium-ion battery charging. J Dyn Syst Meas Control. 2016; 138(2): 021009. https://doi.org/10.1115/1.4032066

[10] Hemavathi S, Kumaran AT. Exploring the thermal landscape: comprehensive insights into Li-ion battery safety and management. ChemBioEng Rev. 2025; 12(2): 1-25. https://doi.org/10.1002/cben.202400037

[11] International Energy Agency. India's market size and global share in clean energy technologies. 2019. Available from: https://www.iea.org (cited 2025 Jan 10).

[12] Anees AS. Grid integration of renewable energy sources: challenges, issues, and possible solutions. In: Proc IEEE 5th India Int Conf Power Electronics (IICPE); 2012. p. 1-6. https://doi.org/10.1109/IICPE.2012.6450514

[13] Hemavathi S. Lithium-ion battery state of health estimation using intelligent methods. Franklin Open. 2025; 10: 100237. https://doi.org/10.1016/j.fraope.2025.100237

[14] India Briefing. Electric vehicle industry in India: Why foreign investors should pay attention. 2019. Available from: https://www.india-briefing.com (cited 2025 Jan 10).

[15] Hemavathi S. Lithium-ion battery state of health estimation using intelligent methods. Franklin Open. 2025; 10: 100237. https://doi.org/10.1016/j.fraope.2025.100237

[16] Kumaran AT, Hemavathi S. Optimization of lithium-ion battery thermal performance using dielectric fluid immersion cooling technique. Process Saf Environ Prot. 2024; 189: 768-1. https://doi.org/10.1016/j.psep.2024.06.117

[17] Choi JW, Aurbach D. Promise and reality of post lithium-ion batteries with high energy densities. Nat Rev Mater. 2016; 1: 16013. https://doi.org/10.1038/natrevmats.2016.13

[18] Hemavathi S, Kumaran AT, Srinivas S, Prakash AS. Synthetic ester-based forced-flow immersion cooling technique for fast discharging lithium-ion battery packs. J Energy Storage. 2024; 97(Pt A): 112852. https://doi.org/10.1016/j.est.2024.112852

[19] Miao Y, Hynan P, von Jouanne A, Yokochi A. Current Li-ion battery technologies in electric vehicles and opportunities for advancements. Energies. 2019; 12(6): 1074. https://doi.org/10.3390/en12061074

[20] Patnaik L, Praneeth A, Williamson SS. A closed-loop constant-temperature constant-voltage charging technique to reduce charge time of lithium-ion batteries. IEEE Trans Ind Electron. 2019; 66(2): 1059-67. https://doi.org/10.1109/TIE.2018.2833038

[21] Hemavathi S, Prakash AS. Exploring the thermal landscape: comprehensive insights into Li-ion battery safety and management. ChemBioEng Rev. 2025; 12(2): e202400037. https://doi.org/10.1002/cben.202400037

[22] Keil P, Jossen A. Charging protocols for lithium-ion batteries and their impact on cycle life-An experimental study. J Energy Storage. 2016; 6: 125-41. https://doi.org/10.1016/j.est.2016.02.005

[23] Hua CC, Lin MY. A study of charging control of lead-acid batteries for electric vehicles. In: Proc IEEE Int Symp Ind Electron (ISIE); 2000. p. 135-40. https://doi.org/10.1109/ISIE.2000.930500

[24] Banguero E, Correcher A, Pérez-Navarro Á, Morant F, Aristizabal A. Review on battery charging and discharging control strategies applied to renewable energy systems. Energies. 2018; 11(4): 1021. https://doi.org/10.3390/en11041021

[25] Hemavathi S, Srinivas S, Prakash AS. Performance evaluation of a hydrostatic-flow immersion cooling system for high-current discharge Li-ion batteries. J Energy Storage. 2023; 72(Pt D): 108560. https://doi.org/10.1016/j.est.2023.108560

[26] Kim JH, Shin JW, Jeon CY, Cho BH. Screening process of Li-ion series battery pack for improved voltage/SOC balancing. In: Proc Int Power Electronics Conf (IPEC); 2010. https://doi.org/10.1109/IPEC.2010.5543534

[27] Xu Y, Ge X, Guo R, Shen W. Active cell balancing for extended operational time of lithium-ion battery systems. arXiv. 2024: 2405.00973. https://doi.org/10.48550/arXiv.2405.00973

[28] Hemavathi S, Srinivas S, Prakash AS. Experimental studies of a static-flow immersion cooling system for fast-charging Li-ion batteries. Exp Heat Transf. 2023; 37(6): 830-50. https://doi.org/10.1080/08916152.2023.2208132

[29] Ouyang Q, Ghaeminezhad N, Li Y, Wik T, Zou C. A unified model for active battery equalization systems. arXiv. 2024:2403.03910. https://doi.org/10.48550/arXiv.2403.03910

[30] Nath A, Gupta R, Mehta R, Bahga SS, Gupta A, Bhasin S. Attractive ellipsoid sliding mode observer design for SOC estimation. arXiv. 2020: 2008.06871. https://doi.org/10.1109/TVT.2020.3035681

[31] Kumaran AT, Hemavathi S. Optimization of lithium-ion battery thermal performance using dielectric fluid immersion cooling. Process Saf Environ Prot. 2024; 189: 768-81. https://doi.org/10.1016/j.psep.2024.06.117

[32] Sultan YA, Eladl AA, Hassan MA, Gamel SA. Enhancing electric vehicle battery lifespan through active balancing and machine learning. Sci Rep. 2025; 15: 777. https://doi.org/10.1038/s41598-024-82778-w

[33] Jiang S, Xiong R, Chen C, Shen W. Estimation of parameters and state of charge for solid-state batteries. IEEE Trans Transp Electrific. 2024. https://doi.org/10.1109/TTE.2024.3446634

[34] Hemavathi S, Jeevandoss CR, Srinivas S, Prakash AS. Temperature distribution analysis during fast discharging of Li-ion battery packs. Heat Transf Res. 2024; 55(2): 41-54. https://doi.org/10.1615/HeatTransRes.2023048880

[35] Smith K, Gasper P, Colclasure A, Shimonishi Y, Yoshida S. Lithium-ion battery life model with electrode cracking. J Electrochem Soc. 2021; 168(10): 100530. https://doi.org/10.1149/1945-7111/ac2ebd

[36] Hemavathi S, Srinivas S, Prakash AS. Present and future generation of secondary batteries: a review. ChemBioEng Rev. 2023; 10(6): 1123-45. https://doi.org/10.1002/cben.202200040

[37] Zhang Z, Zhang L, Hu L, Huang C. Active cell balancing of lithium-ion battery pack based on average SOC. Int J Energy Res. 2020; 44(4): 2535-48. https://doi.org/10.1002/er.4876

[38] Dong B, Li Y, Han Y. Parallel architecture for battery charge equalization. IEEE Trans Power Electron. 2015; 30(9): 4906-13. https://doi.org/10.1109/TPEL.2014.2364838

[39] Zhu L. Li-ion battery active-passive hybrid equalization. Energies. 2025; 18(10): 2463. https://doi.org/10.3390/en18102463

[40] Hemavathi S, Kumaran AT, Srinivas S, Prakash AS. Synthetic ester-based forced-flow immersion cooling technique for fast discharging lithium-ion battery packs. J Energy Storage. 2024; 97(Pt A): 112852. https://doi.org/10.1016/j.est.2024.112852

[41] Praveena Krishna PS, Jayalakshmi NS, Adarsh S, Bagchi S. Switched supercapacitor active cell balancing in lithium-ion battery pack for low-power EV applications. Cogent Eng. 2024; 11(1): 2425741. https://doi.org/10.1080/23311916.2024.2425741

[42] Kumar S, Rao SK, Singh AR, Naidoo R. Switched resistor passive balancing of Li-ion battery pack and estimation of power limits for battery management system. Int J Energy Res. 2023; 2023: 5547603. https://doi.org/10.1155/2023/5547603

[43] Itagi AR, Kallimani R, Pai K, Iyer S, López OLA, Mutagekar S. Cell balancing paradigms: advanced types, algorithms, and optimization frameworks. arXiv. 2024: 2411.05478. doi:10.48550/arXiv.2411.05478.

[44] Hemavathi S, Jeevandoss CR, Srinivas S, Prakash AS. Experimental studies on Li-ion battery pack temperature distribution during fast discharging and varied ambient conditions. Heat Transf Res. 2024; 55(2): 41-54. https://doi.org/10.1615/HeatTransRes.2023048880

[45] Hemavathi S. Overview of cell-balancing methods for lithium-ion battery technology. Energy Storage. 2020;3: e203. https://doi.org/10.1002/est2.203

[46] Hua Y, Zhou S, Huang Y, Liu X, Ling H, Zhou X, *et al*. Sustainable value chain of retired lithium-ion batteries for electric vehicles. J Power Sources. 2020; 478: 228753. https://doi.org/10.1016/j.jpowsour.2020.228753

[47] Liu K, Li K, Peng Q, Zhang C. A brief review on key technologies in battery management system of electric vehicles. Front Mech Eng. 2019; 14(1): 47-64. https://doi.org/10.1007/s11465-018-0516-8

[48] Berecibar M, Gandiaga I, Villarreal I, Omar N, Van Mierlo J, Van den Bossche P. Critical review of state of health estimation methods of Li-ion batteries for real applications. Renew Sustain Energy Rev. 2016; 56: 572-87. https://doi.org/10.1016/j.rser.2015.11.042

[49] Hemavathi S. Modeling of Analog battery management systems for single-cell lithium-ion batteries. Energy Storage. 2020; 3: e208. https://doi.org/10.1002/est2.208

[50] Park SH, Park YG, Ha MY. Numerical study on the effect of tube number and arrangement on melting performance of phase change material in latent thermal energy storage systems. J Energy Storage. 2020; 32: 101780. https://doi.org/10.1016/j.est.2020.101780

[51] Wang S, Hsia B, Alper JP, Carraro C, Wang Z, Maboudian R. Comparative studies on electrochemical cycling behavior of two different silica ionogels. J Power Sources. 2016; 301: 299-305. https://doi.org/10.1016/j.jpowsour.2015.09.121

[52] Hemavathi S, Arumugam T. An overview of the current and future trends in the design and performance of lithium-ion battery packs for electric vehicles. Proc Inst Mech Eng Part A J Power Energy. 2025; 239(8): 1276- 1304. https://doi.org/10.1177/09576509251382717

[53] Hemavathi S. India's lithium-ion battery landscape: strategic opportunities, market dynamics, and innovation pathways. Energy Storage. 2025;7(6): e70244. https://doi.org/10.1002/est2.70244

[54] Devadiga D, Selvakumar M, Shetty P, Santosh MS. Recent progress in dye-sensitized solar cell materials and photo-supercapacitors: A review. J Power Sources. 2021; 493: 229698. https://doi.org/10.1016/j.jpowsour.2021.229698

[55] Kim GH, Pesaran A, Spotnitz R. A three-dimensional thermal abuse model for lithium-ion cells. J Power Sources. 2007; 170(2): 476-489. https://doi.org/10.1016/j.jpowsour.2007.04.018

[56] Hemavathi S, Arun Kumar A. Evaluation of cooling effectiveness for cylindrical and prismatic batteries using oil immersion cooling systems. J Therm Anal Calorim. 2025; 1-18 (epub ahead). https://doi.org/10.1007/s10973-025-14285-7

[57] Guo R, Lu L, Ouyang M, Feng X. Mechanism of entire overdischarge process and overdischarge-induced internal short circuit in lithium-ion batteries. Sci Rep. 2016; 6: 30248. https://doi.org/10.1038/srep30248

[58] Arun Kumar A, Pavithra T, Hemavathi S. Dynamic electrochemical impedance spectroscopy-based diagnosis of electrochemical and thermal behavior in Li-ion batteries under varying current rates, state of charge, and temperature. Adv Sustain Syst. 2025: e00878. https://doi.org/10.1002/adsu.202500878

[59] Waldmann T, Wilka M, Kasper M, Fleischhammer M, Wohlfahrt-Mehrens M. Temperature-dependent ageing mechanisms in lithium-ion batteries: A post-mortem study. J Power Sources. 2014; 262: 129-35. https://doi.org/10.1016/j.jpowsour.2014.03.112

[60] Hemavathi S, Antopaul DA. Design of dielectric fluid immersion cooling system for efficient thermal management of lithium-ion battery packs. Energy Storage. 2025; 7: e70196. https://doi.org/10.1002/est2.70196

[61] Ma S, Jiang M, Tao P, Song C, Wu J, Wang J, Deng T. Temperature effect and thermal impact in lithium-ion batteries: A review. Prog Nat Sci Mater Int. 2018; 28(6): 653-66. https://doi.org/10.1016/j.pnsc.2018.11.002

[62] Liu H, Wei Z, He W, Zhao J. Thermal issues about Li-ion batteries and recent progress in battery thermal management systems: A review. Energy Convers Manag. 2017; 150: 304-30. https://doi.org/10.1016/j.enconman.2017.08.016

[63] Bandhauer TM, Garimella S, Fuller TF. A critical review of thermal issues in lithium-ion batteries. J Electrochem Soc. 2011; 158(3): R1-R25. https://doi.org/10.1149/1.3515880

[64] Xu B, Oudalov A, Ulbig A, Andersson G, Kirschen DS. Modeling of lithium-ion battery degradation for cell life assessment. IEEE Trans Smart Grid. 2018; 9(2): 1131-40. https://doi.org/10.1109/TSG.2016.2578950